Intracellular pH sensor based on heteroleptic bis-cyclometalated iridium(III) complex embedded into block-copolymer nanospecies: application in phosphorescence lifetime imaging microscopy

Julia R. Shakirova, Vadim A. Baigildin, Anastasia I. Solomatina, Reza Babadi Aghakhanpour, Vladimir V. Pavlovskiy, Vitaly V. Porsev, and Sergey P. Tunik**

J.R. Shakirova, V.A. Baigildin, A.I. Solomatina, R.B. Aghakhanpour, S.P. Tunik
Department of general and inorganic chemistry, Institute of Chemistry, St. Petersburg State University, St. Petersburg, 198504, Russia
E-mail: y.r.shakirova@spbu.ru, sergey.tunik@spbu.ru

Vladimir V. Pavlovskiy, Vitaly V. Porsev
Department of quantum chemistry, Institute of Chemistry, St. Petersburg State University, St. Petersburg, 198504, Russia

Keywords: phosphorescent pH sensors, intracellular pH, phosphorescence lifetime imaging microscopy, cyclometalated iridium complexes, RAFT-polymeric nanoparticles

Herein we report on a novel pH-responsive phosphorescent probe based on cyclometalated iridium(III) complex. To prevent oxygen quenching of phosphorescence and to improve the probe biocompatibility, the complex is covalently conjugated with a water-soluble block-copolymer that also increases its pH sensitivity. The resulting polymeric nanoprobe demonstrates a strong response of the phosphorescence lifetime onto pH variations in physiological range. Cellular experiments with Chinese hamster ovary (CHO-K1) cells show the predominant internalization of the probe in acidified cell compartments, endosomes and lysosomes. The analysis of phosphorescence lifetime imaging microscopy (PLIM) data confirms applicability of the sensor for monitoring of intra- and extracellular pH in cell cultures.

1. Introduction

pH is a key physiological parameter of biological systems, which regulates a wide range of processes at cell level both in healthy and abnormal tissues. The synthesis and degradation of biomolecules as well as traffic of biocomponents may effectively occur only at specific pH

values,[1,2] and deviations from the ones «normal» for the corresponding organs/tissues/cells/cell compartments indicate their dysfunctions such as renal failure,[3] cancer[3,4] or apoptosis.[5] Furthermore, response to therapies may be also assessed by the measurements of intra- and/or extracellular pH[6,7] that provides important pharmacological information. Therefore, real time monitoring of pH in biological samples is of critical importance both for the fundamental biology and experimental medicine as well as for diagnosis of various diseases. In this field optical sensors based on the luminescence response to variation in pH are the most convenient tools, in particular, for obtaining information at microscopic level because this technique is non-invasive, displays high spatiotemporal resolution, shows reversible response that makes possible real time monitoring of the target parameter.[8–11] So far, the majority of the sensors used to monitor intra- and extracellular pH are the fluorescent molecular probes containing pH-sensitive functional groups in the nearest environment of the chromophore.[8,11] There are three major modalities to acquire the probe response onto variations in pH, namely, emission intensity in absolute and ratiometric modes[12–14] and lifetime measurements.[15] Two former approaches are based on observations of the sensor signal intensity and therefore suffer from the dependence of their results on the optical properties of the samples under study. This is particularly relevant to the absolute mode, the readings of which depend not only on pH, but also on the concentration of the probe that can significantly impair the accuracy of determined pH values at a quantitative level. Ratiometric fluorescent pH sensors of various nature (small molecules, nanoparticles, metal-organic frameworks, genetically encoded fluorescent proteins) are now widely used in biological research,[15–19] where small molecules-based sensors dominate because they are relatively inexpensive, convenient to handle, readily internalize in cells, and allow targeted chemical design for application in the studies of different biosamples.

On the contrary, the latter mode based on emission lifetime is independent of the biasing factors typical of emission intensity measurements and is now getting an important way to detect the sensor response onto target external stimuli. In the recent decade the development of time-resolved luminescent microscopy (for example, fluorescence-lifetime imaging microscopy (FLIM) technique[20–23]) made possible application of fluorescent probes in quantitative analysis of key physiological parameters in living cells. FLIM pH sensors constitute a considerable part of this family and include small organic molecules[15,17,24–26] and genetically encoded fluorescent proteins.[18,27–30] However, similar to many other fluorescent probes these sensors have some inevitable drawbacks related to their natural photophysical properties, namely, small Stokes shift, which results in the interference of background

emission, and low bleaching stability. The both shortcomings can be overcome by using the phosphorescent emitters, which display inherently large Stokes shifts, high bleaching stability and commonly provide rich opportunities for modification of their photophysical and physico-chemical properties. Additionally, phosphorescence lifetime in microsecond domain ensures a wider interval of measurable values together with more convenient and less expensive ways to carry out data acquisition compared to the measurements of nanosecond lifetimes typical for fluorescent emitters. These considerations attract growing attention to the phosphorescent transition metal complexes as potentially applicable sensors for a wide range of bio-environment characteristics, see recent reviews.[29,31,32] Nevertheless, it is worth noting that their luminescence can be effectively quenched by molecular oxygen that is determined by the triplet-triplet energy transfer between the ground state of the O_2 molecule and the excited state of phosphorescent emitters. For this reason, to date, phosphorescent complexes have been predominantly used as a major instrument for monitoring of oxygen concentration in biological systems[33–37]. The phosphorescent complexes containing pH-responsive functions (-COOH, -NR_2, -OH) in the ligand environment may also display the response of luminescent characteristics (intensity, lifetime) to media pH variations and thus can be used as pH sensors.[33,38–45] However, the inherent sensitivity of the phosphorescent pH sensors to molecular oxygen inevitably results in the crosstalk between two external stimuli (O_2-pH), the both may considerably vary in live biological objects. The examples of the phosphorescent pH sensors application in biological studies[38,39,45–48] either demonstrate their application as on/off indicators in a certain pH interval[39,46,47] or implicitly assumed an even oxygen distribution across the sample and its pressure equal to that in the system used for the sensor quantitative calibration.[38,45,48] This is not necessarily true for living biological systems that is clearly mentioned in one of these publications.[45] To avoid this biasing crosstalk, it is possible to use pH sensitive emitters based on lanthanide complexes,[49–52] the emission of which is not quenched by oxygen and show both large Stokes shift and long lived (10^2-10^3 μs) emission. Nevertheless, it is hard to use the lanthanide complexes in physiological media because many of them suffer from strong emission quenching with water molecules that considerably complicates weak signal detection. Moreover, in the case of experiments performed in phosphorescence lifetime imaging (PLIM) mode so large lifetimes (up to a few ms) hamper real time-data acquisition in living biosamples.

In our study, we decided to use the phosphorescent iridium complexes showing strong lifetime dependence on pH in physiologically relevant interval as practically applicable lifetime-based biosensors. To eliminate the crosstalk of pH response with the variations in

oxygen concentration, the sensor's chromophore has been embedded into polymeric nanospecies permeable for protons and impermeable for oxygen molecules. The obtained nanosensor displays strong response of the phosphorescence lifetime onto pH in the physiologically important interval and negligible response to other physiological parameters such as oxygen concentration, salinity, the presence of Ca^{2+} and Mg^{2+} cations. It was also demonstrated that the presence of biomacromolecules such as fetal bovine serum (FBS) increases the lifetimes values but does not significantly change the probe sensitivity that made possible to use the calibration curve built up in the cultural media for determination of the intercellular pH values.

2. Results and discussions

2.1. Iridium(III) complexes: synthesis and photophysical studies

2.1.1. Synthesis and characterization of complexes

The heteroleptic cationic Ir(III) complexes of the $[(N^C)_2Ir(N^N)]^+$ type have been synthesized by a standard methodology[42,53–55] (**Scheme 1**): N^C = methyl 2-phenylquinoline-4-carboxylate; N^N = 4-(2-(3-bromophenyl)-1H-imidazo[4,5-*f*][1,10]phenanthrolin-1-yl)benzoic acid (**Ir-OMe**), 2,5-dioxopyrrolidin-1-yl 4-(2-(3-bromophenyl)-1H-imidazo[4,5-f][1,10]phenanthrolin-1-yl)benzoate (**Ir-Su**). The ester groups in the cyclometalated ligands of **Ir-OMe** were hydrolyzed in the presence of sodium carbonate to give the water-soluble complex **Ir-ONa**, protonation of which with the hydrochloric acid leads to the formation of the **Ir-OH** complex.

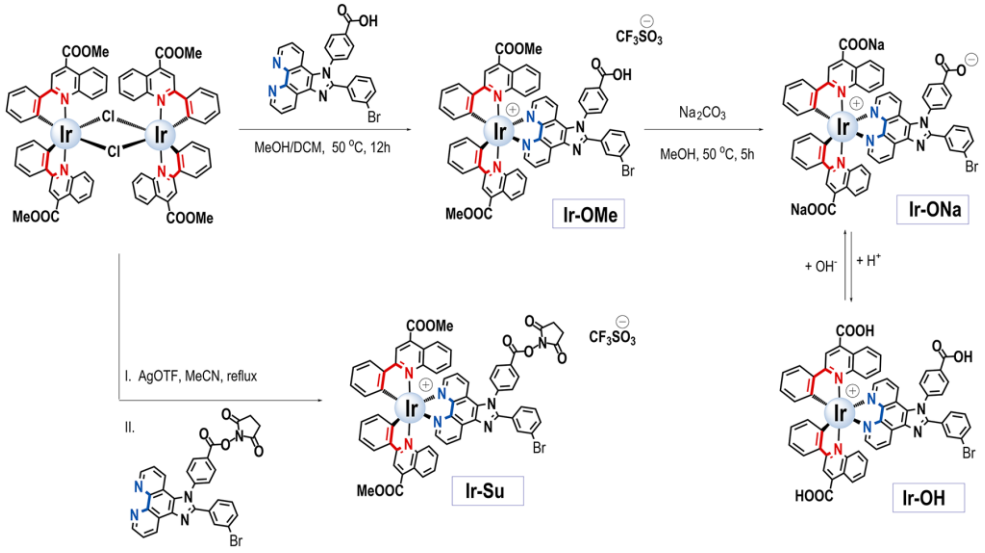

Scheme 1. Synthesis of the iridium(III) complexes.

The N^N ligands and complexes were thoroughly characterized by NMR spectroscopy, mass-spectrometry, and elemental analysis, see Experimental and Figure S1-S11 (Supporting Information). According to the spectroscopic data obtained, the general structural motif of these iridium complexes corresponds to the "classic" environment of the metal center: the octahedral geometry of Ir(III) is formed by two cyclometalating ligands with *cis*-oriented Ir–C bonds and one N^N ligand in the *trans* position relative to the carbon atoms of the N^C chelates. The DFT optimized structures (**Figure 1**) agree with the spectroscopic data, and the corresponding structural patterns shown in Scheme 1.

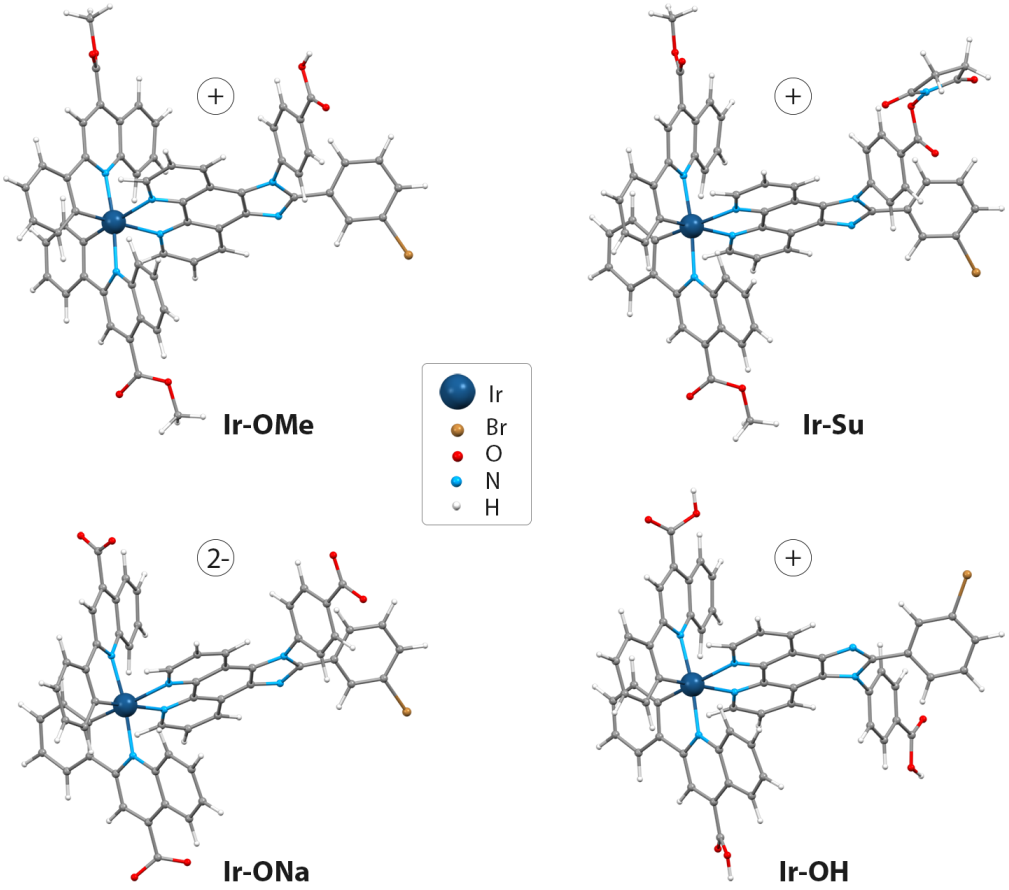

Figure 1. Optimized structures of iridium(III) complexes.

2.1.2. Photophysical study of complexes

Photophysical properties of the complexes were studied in methanol and aqueous (in the case of **Ir-ONa** and **Ir-OH**) solutions. The numerical data are summarized in **Table 1**, excitation and emission spectra are shown in **Figure 2**, absorption spectra are shown in Figure S12 of the Supporting Information.

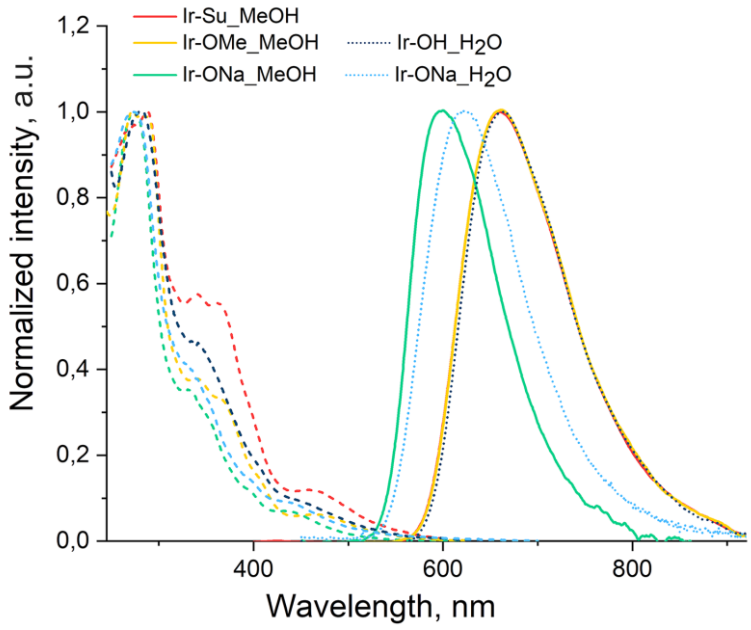

Figure 2. Excitation and emission spectra of iridium complexes (**Ir-Su, Ir-OMe, Ir-ONa, Ir-OH)** in methanol and water solutions, 298K.

Table 1. Photophysical properties of complexes in methanol and aqueous solutions, 298K.

	λ_{abs} *(ε*10^{-3} [l*mol^{-1}*cm^{-1}])* [nm]	λ_{exc} [nm][a)]	λ_{em} [nm][b)]	$\Phi_{aer/deg}$ [b)]	$\tau_{aer/deg}$ [µs] [a) b)]
Methanol solution					
Ir-OMe	270 *(92)*, 282 *(89)*, 340 *(39)*, 363 *(30)*, 400sh *(16)*, 467 *(5.5)*	273, 283, 341, 365, 403, 466	660	0.03/0.05	0.14/0.24
Ir-Su	268 *(90)*, 287sh *(81)*, 346 *(28)*, 363 *(27)*, 400sh *(12)*, 463 *(4)*	287, 342, 363, 463	660	0.07/0.11	0.14/0.24
Ir-ONa	277 *(83)*, 330sh *(32)*, 366sh *(22)*, 397sh *(11)*, 441 *(6)*	274, 330, 441	600	0.09/0.30	0.43/1.61
Aqueous solution					
Ir-ONa (pH = 8)	273 *(90)*, 330sh *(37)*, 366sh *(22)*, 394sh *(13)*, 436 *(8)*	273, 330, 436	620	0.03/0.04	0.25/0.32
Ir-OH (pH = 3)	279 (*61*), 346 (*28*), 396sh (*13*), 456 (*5.5*)	282, 336, 448	660	0.01/0.02	0.12/0.15

[a)]measured at λ_{em} = 650 nm; [b)]λ_{exc} = 351 nm.

In methanol solution, the obtained complexes display strong high-energy absorption band at ca. 300 nm and two lower-energy shoulders (ca. 350 and 450 nm) at the band tail extending up to 550 nm. DFT analysis of the transitions observed in these spectra shows that for the complexes containing non-ionisable –C(O)OMe groups in the N^C ligands (**Ir-OMe, Ir-Su**) the character of the high and low energy absorption bands are represented by a complex

mixture of the ligand centered (^{1}LC, (N^C)), interligand (^{1}LLCT, (π(N^C)→π*(N^C')), and metal-to-ligand (^{1}MLCT, d(Ir)→π*(N^C)) transitions with the excited states localized mainly at the aromatic systems of the N^C ligands, see Figure S13-S16, Table S1-S8, Supporting Information. From the viewpoint of interpretation of the chromophore spectroscopic response onto variations in pH, it is of essential interest to compare the nature of singlet transitions in the **Ir-ONa**, **Ir-OH** complexes, which are the counterparts of the deprotonation/protonation reactions in aqueous media. Analysis of the computational results (see **Figure 3**, Figure S17-S21, Table S9-S17, Supporting Information) revealed substantial difference in the excited state character in these species. The behavior of the protonated **Ir-OH** molecule is essentially similar to that of the non-ionisable chromophores where one can observe negligible participation of the N^N ligand orbitals in generation of the singlet excited states. On the contrary, in completely deprotonated **Ir-ONa** species the charge transfer from the metal ion and N^C ligands orbitals to the N^N ligand proved to play a key role in the lowest energy transitions and determines the character of these singlet excited states. For the sake of comparison, we also performed calculations for the partly protonated **Ir-OH/ONa** species (Figure 3_top) that indicate that the character of the lowest excited state for partly protonated chromophore is closer to that found for completely protonated **Ir-OH** species. The excited state transformation upon deprotonation of the carboxylic group is evidently associated with the difference in the donor properties of the carboxylic group and its deprotonated form (carboxylate anion); the former is a moderate electron-withdrawing group with both negative mesomeric (-M) and inductive (-I) effects, whereas the latter demonstrates weak +I effects.[54]

All complexes demonstrate emission in the orange to red spectral region with large Stokes shift, lifetime in microsecond domain, and substantial emission quenching by molecular oxygen (Figure 2 and Table 1) that indicate luminescence from triplet excited states, i.e., phosphorescence. According to the results of the DFT and TD DFT calculations emission in the complexes **Ir-OMe**, **Ir-Su**, and **Ir-OH** occurs from the triplet state of the mixed character (^{3}LC, ^{3}ILCT, and ^{3}MLCT) with predominant localization at the N^C ligand orbitals (Figure 3_bottom, Figure S21-S22, Table S18-S23, Supporting Information). Similar to the variations in the nature of the lowest singlet excited state, *vide supra*, the **Ir-ONa** complex with deprotonated carboxylic groups displays emissive transition from the triplet excited state localized mainly at the N^N ligand (Figure 3_bottom, Figure S21, Table S19, Supporting Information.

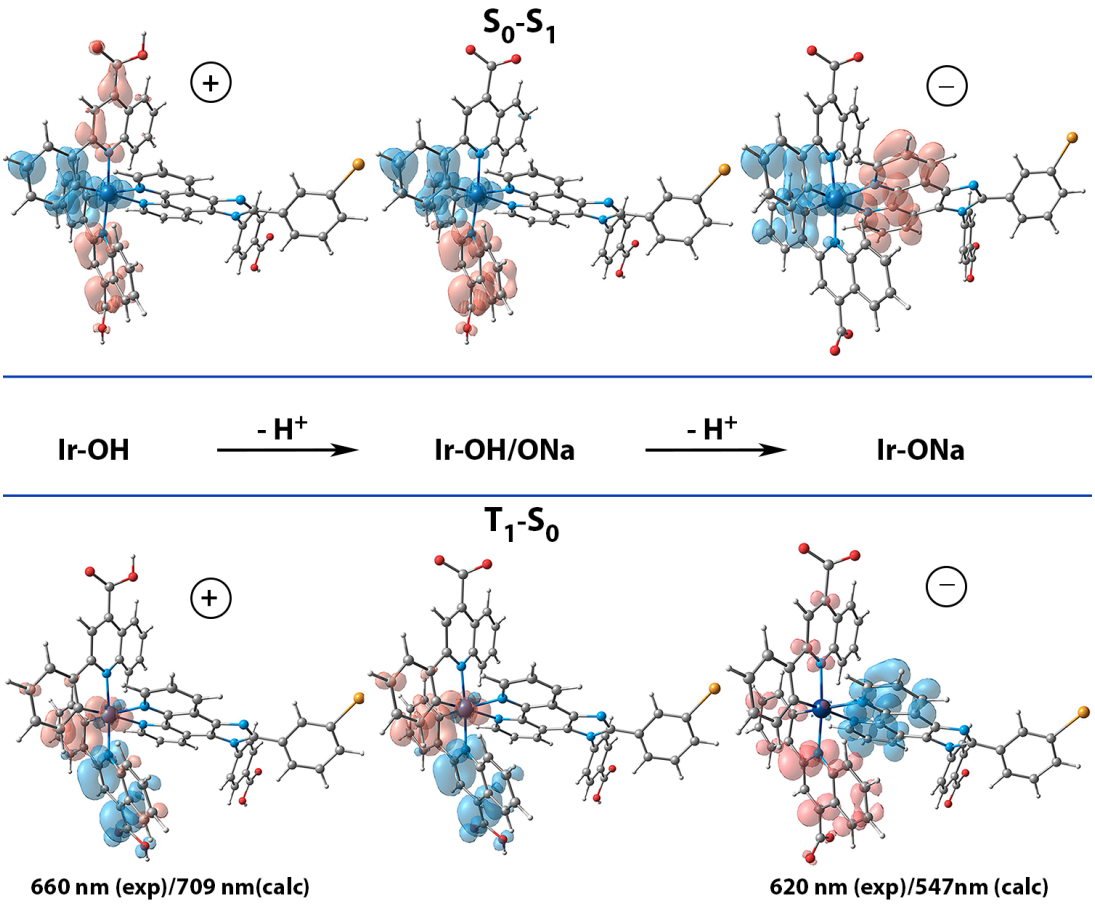

Figure 3. Electronic density transfer (blue – depletion, red – increase) in the S_0-S_1 and T_1-S_0 transitions of protonated (**Ir-OH**), partially deprotonated (**Ir-OH/ONa**) and fully deprotonated (**Ir-ONa**) complexes.

The positive solvatochromism of Ir-ONa emission when methanol is replaced by highly polar aqueous media also indicates a significant contribution of charge transfer character into emissive excited state (Figure 2).[56–58] It is also worth noting that deprotonation reaction is accompanied by a blue shift of emission band maximum and considerable changes in the emission intensity and lifetime values (**Figure 4**) that is indicative of potential applicability of these complexes for monitoring of pH variations in aqueous solutions both in the intensity and lifetime modes.

The dynamic equilibrium between **Ir-ONa** and **Ir-OH** in aqueous solutions obviously depends on the concentration of protons providing pH-dependent emission intensity in the physiologically relevant range (Table 1, Figure 4a), similar to the previously studied analogues.[42,54,59] Emission decay measured at the wavelength of ca. 650 nm (the intermediate point between the maxima of emission bands corresponding to protonated (**Ir-OH**) and deprotonated complexes (**Ir-ONa**)) can be fit with monoexponential function to

give a clear dependence of the lifetime on pH in the range 2.0 – 9.0 with the lifetime values (τ) variations from 0.11 μs to 0.31 μs for aerated solution and the pK_a value of ca. 6.5. (Figure 4b, Table S24, Figure S23, Supporting Information). It should also be mentioned that in biologically relevant pH range (5.0 – 8.0) the dependence is nearly linear (Figure 4b).

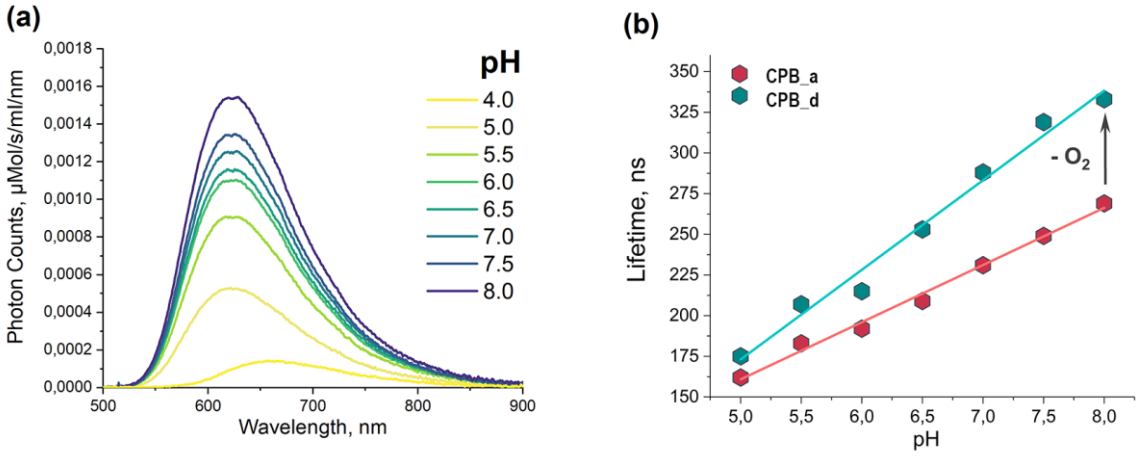

Figure 4. a) Emission spectra of the complex **Ir-ONa** in citrate-phosphate buffer solution at different pH values, 298 K, λ_{exc} = 365 nm. b) Lifetime *vs* pH graphs in aerated (red spots) and deaerated (green spots) PB and CB solutions measured at λ_{em} = 650 nm, 298 K.

Not surprisingly, the emission lifetime and intensity of **Ir-ONa** also depends on the presence of molecular oxygen, which is a natural quencher of phosphorescent emitters. Figure 4b shows that the difference in the lifetimes of aerated and deoxygenated solutions of **Ir-ONa** in the pH range 5.0 – 8.0 may amount up to 35% under basic conditions that is unacceptable for quantitative pH determination in complex biological systems with unpredictable content of oxygen.

To solve the key problem of the phosphorescent pH sensors, i.e., to protect the chromophore from quenching by oxygen, we decided to covalently conjugate the pH sensitive emitter to water-soluble block-copolymer, which could form a kind of shell around the chromophore thus shielding the emitter from collisions with the quencher molecules. However, this shell should not break the protonation/deprotonation equilibrium of the sensor keeping intact the emitter response onto pH variations. Additionally, embedding of emitter into polymeric nanoconjugate is also aimed at enhancement of the sensor biocompatibility and water-solubility as well as at protection of the chromophore from interaction with biological microenvironment, which can also distort the lifetime response onto the target external stimuli. The most promising candidates are hydrophilic polymers that can self-assemble into tightly packed macromolecular chains in aqueous solution. Keeping this in mind, we chose

the RAFT polymerization technique[60] as a strategy to obtain a biocompatible copolymer as a carrier for the pH-sensitive phosphorescent complex. This approach gives a degree of freedom in variations of the copolymer composition and properties also making possible different methods of the iridium emitter conjugation to the polymer. To perform the conjugation, we introduced activated N-hydroxysuccinimidyl ester group into the periphery of the N^N ligand (**Ir-Su** complex, Scheme 1), which is able to form the amide bond upon interaction with amino groups of the block-copolymer under mild conditions.

2.2. Synthesis of Block-Copolymer and complex conjugation

*2.2.1. Synthesis of block-copolymer and its conjugate with Iridium(III) complex (**BC-Ir**)*

For the copolymer synthesis, *N*-vinylpyrrolidone **(VP)** and *N*-vinylformamide (**VFA)** were chosen as both monomers are widely used in biomedical applications[61,62] due to their long-term stability, low toxicity, and simple approaches to the syntheses of biocompatible water-soluble polymers.[62–64] **VFA** can be hydrolyzed to give amino-containing units,[65] thus opening the way to the polymer conjugation with the iridium complex *via* interaction with the activated N-hydroxysuccinimidyl ester group. Polyvinylpyrrolidone (**p(VP)**) was also chosen because it demonstrates a reduced oxygen permeability[66] that can potentially eliminate the phosphorescence quenching of the iridium chromophore by molecular oxygen.

The synthetic route and chemical structure of amino groups containing block-copolymer **BC-NH$_2$** are shown in **Scheme 2**. At the first step, **p(VP)** was synthesized via the RAFT polymerization, and its structure was characterized by ^{1}H NMR spectroscopy (Figure S24a, Supporting Information). Mass average molecular weight M_w of **p(VP)** was determined to be 37 100 Da with the polydispersity index of 1.69 measured using GPC with the calibration curve of pullulan standards (Figure S25, Supporting Information). At the next step **VFA** units were copolymerized to **p(VP)**; in this reaction the latter acts as the macro-RAFT agent to give the poly-(vinylpyrrolidone-block-vinylformamide) (**p(VP-b-VFA)**) product, which was characterized by the ^{1}H NMR spectroscopy (Figure S24b, Supporting Information) and gel-permission chromatography (GPC), Figure S25, Supporting Information. The ^{1}H NMR spectrum of **p(VP-b-VFA)** confirms the formation of the block-copolymer by the appearance of the proton signals at ca. 7.95 [NH-C(O)H], 3.84 (C-H) (Figure S24b, Supporting Information). Comparing the peak area of these protons, we estimated the **VP** to **VFA** units molar ratio as ca. 80:20. This result is in good agreement with the product molecular weight M_w of 42 600 Da determined by GPC with the polydispersity of 1.75 (Figure S25, Supporting Information). The final step of the copolymer synthesis consisted in the hydrolysis of the

VFA formamide functions to give amino-containing units in the copolymer chain. The disappearance of the formyl proton signals in the ^{1}H spectrum of the block-copolymer after hydrolysis also confirms the formation of the poly(vinylpyrrolidone-block-vinylamine) copolymer designated as **BC-NH$_2$** (Scheme 2, Figure S24c, Supporting Information).

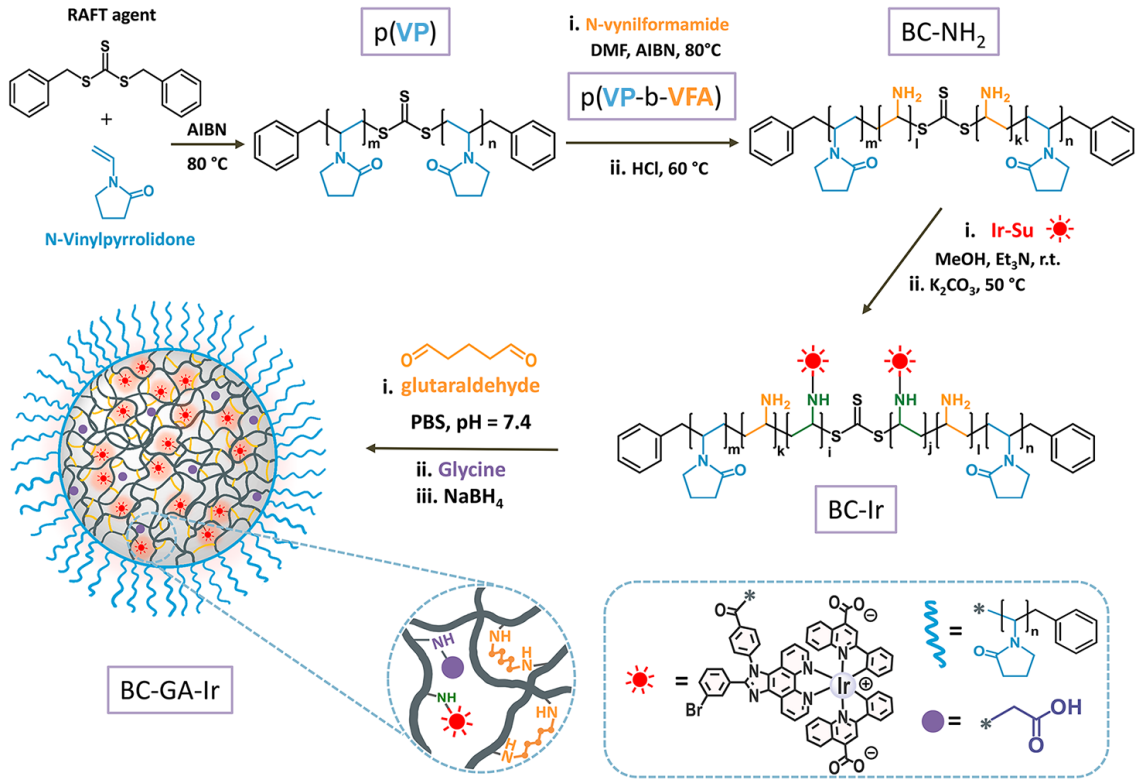

Scheme 2. Synthesis of block-copolymer and conjugates.

The conjugation of the **Ir-Su** complex and **BC-NH$_2$** (Scheme 2) was performed in methanol in the presence of base with an equimolar ratio of reacting groups (Su:NH$_2$ = 1:1). At the second stage, hydrolysis of the iridium complex ester groups was carried out *in situ* in the presence of potassium carbonate, followed by dialysis and lyophilization. The **BC-Ir** conjugate possesses an amphiphilic structure: the block of **p(VP)**-chains is hydrophilic while the conjugated iridium complex brings hydrophobicity to the corresponding part of the copolymer. Thus, the resulting conjugate, **BC-Ir**, spontaneously aggregates into micelles in aqueous solutions with the hydrodynamic diameters of 33 nm (pH 7.4), 66 nm (pH 10.1), and 22 nm in methanol (**Figure 5**a, Figure S26a, c; Supporting Information). The dependence of the **BS-Ir** ζ-potential on pH was measured in a 10^{-3} M NaCl solution (Figure 5b). The isoelectric point of **BC-Ir** localizes at pH 7.4 that evidences the presence of residual unreacted NH$_2$-groups.[67]

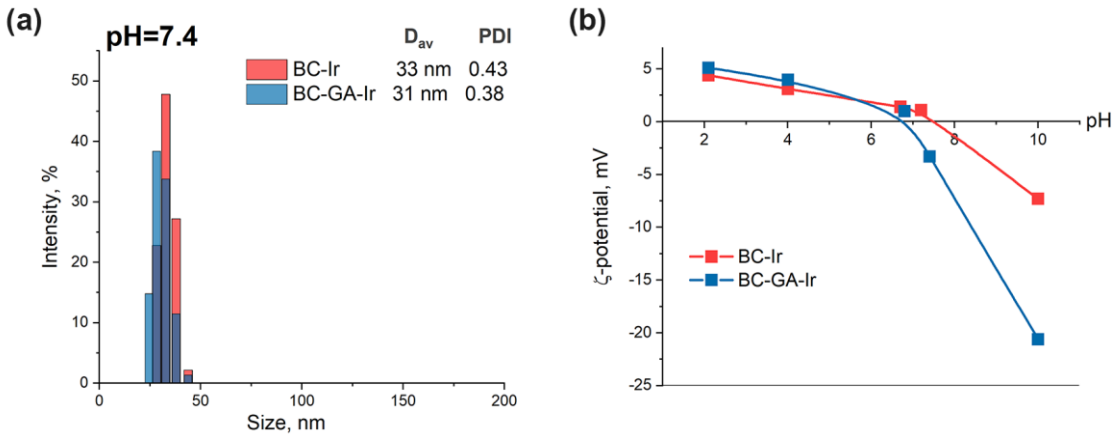

Figure 5. (a) Hydrodynamic diameter of the micelles before and after cross-linking in 10^{-3} N sodium chloride at pH=7.4. (b) The dependence of ζ-potential of the micelles on pH before and after cross-linking.

To further eliminate the quenching effect of oxygen and the influence of the components of biological systems onto the sensor emission characteristics, we applied the strategy of the polymer chains cross-linking in the conjugate by using glutaraldehyde (GA),[68] see Scheme 2. This chemistry rigidifies the nanospecies core, thus, preventing oxygen diffusion inside the species and limits other side effects of the microenvironment in physiological media. The cross-linking of residual amino groups was performed at pH 7.4 that corresponds to the isoelectric point of initial **BC-Ir** conjugate. It is well known[69] that imine bonds formed upon crosslinking and residual aldehyde groups are toxic, therefore glycine and sodium borohydride were used as aldehyde blocking reagents to reduce this effect.[70] Such treatment also increases the biocompatibility of the conjugate, enhance its resistance to hydrolysis, and proved to show no effect onto the emitter photophysical properties.

Cross-linking displays a clearly visible effect onto colloid characteristics of the obtained nanospecies. The hydrodynamic diameter of **BC-GA-Ir** is almost unchanged in aqueous media at pH 7.4 and in methanol solution compared to that of **BC-Ir** (Figure 5a, Figure S26a,b, Supporting Information), but it significantly differs at pH 10.1 (46 nm for **BC-GA-Ir** *vs.* 66 nm for **BC-Ir**) where all amino groups are deprotonated (Figure S26a, Supporting Information). Moreover, the isoelectric point is shifted to more acidic pH of 6.8 (Figure 5b) that also evidences the decrease in amino groups concentration on the surface of **BC-GA-Ir**. Stability of the nanoparticles under acidic (pH 3.8) and neutral (pH 7.4) conditions was also tested by monitoring hydrodynamic diameter and polydispersity index within 24 hours. All these parameters remain practically constant during this period that indicates the stability of

the nanoprobe and the absence of aggregation processes (Figure S27, Supporting Information).

*2.2.2. Photophysical study of **BC-Ir** and **BC-GA-Ir***

The **BC-Ir** and **BC-GA-Ir** conjugates are water-soluble and luminescent both in methanol and aqueous solutions giving a broad emission band centered at ca. 600 nm; absorption, excitation, and emission spectra are shown in Figure S28 and S29a of the Supporting Information.

Table 2. Photophysical properties of BC-GA-Ir in methanol and aqueous solutions.

	λ_{abs} [nm]	λ_{exc} [nm][a)]	λ_{em} [nm][b)]	$\Phi_{aer/deg}$ [b)]	$\tau_{aer/deg}$ [µs] [a) b)]
Methanol solution, 298K					
BC-GA-Ir	275, 335, 351sh, 397sh, 441	274, 327, 438	600	0.05/0.15	0.49/1.73
Aqueous solution, 310K					
BC-GA-Ir (pH = 8.2)	261, 335sh, 436 [c)]	278, 335, 436	615	-	1.00/1.10
BC-GA-Ir (pH = 3.3)	261, 338, 450 [c)]	282, 37sh, 352, 450	645	-	0.16/0.17

[a)]measured at λ_{em} = 650 nm; [b)]λ_{exc} = 351 nm; [c)] absorption spectra in aqueous dispersions are poorly resolved due to high light scattering.

The lifetimes of **Ir-ONa** (Table 1) and **BC-GA-Ir** (Table 2) in aerated and deaerated methanol solutions are essentially similar with small increase of both magnitudes for the conjugated samples. The absence of a significant effect of the polymer on the photophysical properties of the chromophore can be explained by the nature of the solvent and its influence onto the conformation of polymer chains. The chains form the micelles with the core (cross-linked polyvinylamine with conjugated iridium complex) and shell (p(VP) chains) structure, the properties of which depends on the specific interaction of each block with solvent.[71,72] As the affinity of methanol toward the shell-forming block p(VP) is lower compared to water, the chains will adopt less stretched conformation that leads to the decrease in the hydrodynamic micelle size compared to water solutions (Figure S26b, Supporting Information). On the other hand, the affinity of the complex as a more hydrophobic block to methanol leads to swelling and additional chain stretching of micellar core.[72] Thus, the micelles as a whole get less dense that, in turn, increases the oxygen permeability and, consequently, results in high emission lifetime response onto variations in oxygen concentration in methanol.

On the contrary, the reverse situation is observed in aqueous solution: the more hydrophilic shell-forming chains of p(VP) are stretched and the hydrodynamic diameter increases. The hydrophobic core, in contrast, shrinks in water and its low swelling ratio results in significant

diffusion barriers to oxygen penetration.[73] This is the reason of drastic changes in the behavior of emission lifetimes of the conjugate in comparison with non-conjugated complex. At low pH values the lifetimes of **Ir-OH** and **BC-GA-Ir** are nearly the same, while at higher pH the difference becomes obvious (1.0 μs *vs.* 0.25 μs for **BC-GA-Ir** and **Ir-ONa** respectively) and what is even more important the emission quenching by oxygen for the conjugate becomes almost negligible, see Table 2. Thus, the strategy of iridium chromophore packing into this block-copolymer looks promising, in particular, because of reduced oxygen sensitivity and enhanced **BC-GA-Ir** sensitivity to pH compared to the "naked" **Ir-ONa**, *vide infra*.

It is also worth noting that spatial and temporal variations in oxygen concentration in biological samples are far less compared to those between aerated/degassed solutions that additionally decreases the distorting effect of oxygen quenching onto the results of lifetime measurements.

*2.2.3. Photophysical study of **BC-GA-Ir** at various pH*

The cross-linked **BC-GA-Ir** probe demonstrates pH-dependent emission intensity and lifetime in the physiologically relevant range (Figure 6a,b, Figure S29b, Supporting Information). Like the original **Ir-ONa** molecular chromophore, the polymeric **BC-GA-Ir** probe increases the intensity and energy of the emission band upon an increase in pH (Figure 6a). Additionally, the luminescence spectrum of **BC-GA-Ir** displays a weak fluorescent band at 410 nm, related to aggregation induced emission of **p(VP)**[74] in the conjugate (Figure S30, Supporting Information) that, in principle, makes possible ratiometric pH measurements. Nevertheless, data acquisition in lifetime domain gives considerable advantages for quantitative pH monitoring in complex biological systems, *vide supra*, therefore we collected the lifetimes response of **BC-GA-Ir** onto pH variations in different media under aerated and deoxygenated conditions. The obtained data are summarized in Figure 6b, Table S26 and S27 in Supporting Information.

The experiments were carried out in phosphate buffer saline (PBS, pH range 5.0 – 8.0) and Citrate-Phosphate Buffer (CPB, pH range 2.0 - 12.0) solutions. In the media that does not contain biomolecules, the emission of **BC-GA-Ir** shows bi-exponential decay with the average lifetimes (τ_{av}) variations from 0.16 μs to 1.12 μs within the pH range of 3.2-10.0 (Table S25, Figure S31, Supporting Information) regardless of the buffer composition. Despite the increase in the **BC-GA-Ir** emission lifetime compared to the initial complex, the pKa value of the conjugate calculated from the data for CPB solutions remains unchanged at

approximately 6.5 (Figure S31). It is also worth mentioning that the presence of Ca^{2+} and Mg^{2+} ions at the concentration of 0.001M and salinity of 0.1M NaCl does not affect the lifetime response of the conjugate, see Figure 6b and Table S25 of the Supporting Information, that is of particular importance for its application in biological systems, which are abundant in these bio-cations. We also performed additional experiments on the stability of nanoparticles under acidic conditions by monitoring the emission lifetime of the studied sample in buffer solution (pH = 3.9) over 24 hours and tested the reversibility of the emission lifetime response by changing the acidity of the medium between two pH values 5.3 and 7.7 (Figure S27, Supporting Information). In both experiments, we obtained a very good reproducibility that indicates the stability of the nanoprobe.

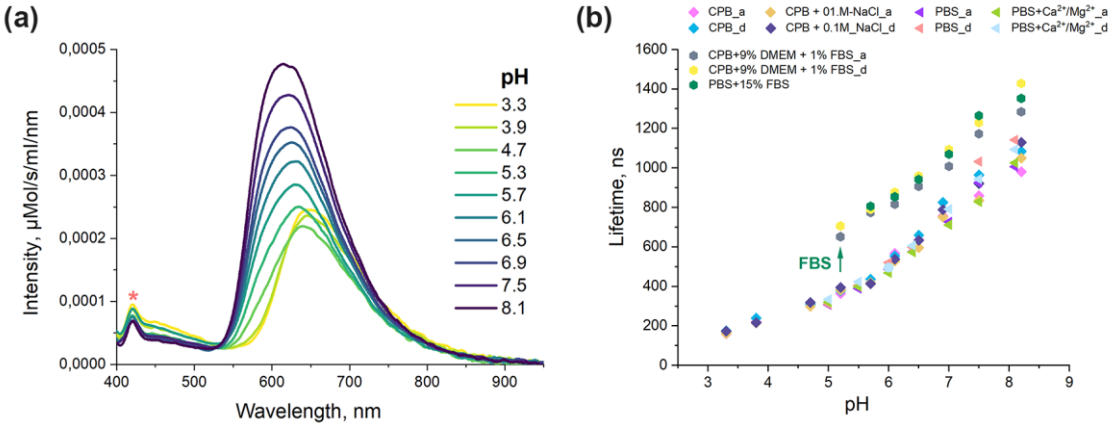

Figure 6. (a) Emission spectra of **BC-GA-Ir** in Citrate-Phosphate Buffer (CPB, pH 3.3 – 7.5) and Phosphate Buffered Saline (PBS, pH 8.1) buffer solutions at different pH values, 310 K, λ_{exc} = 351 nm. * notes sharp signal associated with Raman scattering; (b) pH-lifetime dependence for **BC-GA-Ir** in different media measured at λ_{em} = 650 nm.

As demonstrated by the data shown in Figure 6 b, the effect of oxygen quenching is significantly reduced for the nanospecies to give negligible difference in the probe average lifetimes. Higher deviation was found at pH 7.5 and 8.2 that may be assigned to the deprotonation of carboxylic groups of iridium emitter in the nanosensor. The deprotonation causes, on the one hand, the change of isoelectric potential from positive to negative (Figure 5b), on the other hand, it leads to repulsion between chromophore molecules further resulting in the increase of hydrodynamic diameter (Figure S26a, Supporting Information) and permeability of the nanospecies.

However, it was found that the lifetime calibration on pH in the model physiological media containing 15% or even 1% of fetal bovine serum (FBS) and DMEM shows considerable deviations from the calibration curves obtained in the absence of these biocomponents (Figure

6b, hexagons). This effect can be assigned to the interaction of the sensor with the biomolecules presented in this type of media. Unfortunately, decrease in pH below 5.2 results in FBS aggregation/denaturation visually observed as formation of a bulky precipitate that prevents calibration measurements in this media under acidic conditions.

Although we still observe the influence of biomacromolecules on the lifetime response, the reproducibility of the calibration data from batch to batch and its independence on the concentrations of FBS (1% and 15% of the total volume) prompted us to use all the data obtained in the model physiological media to build up the general calibration of **BC-GA-Ir** emission lifetime as a function of pH in the range of 5.2-8.2. (**Figure 7**).

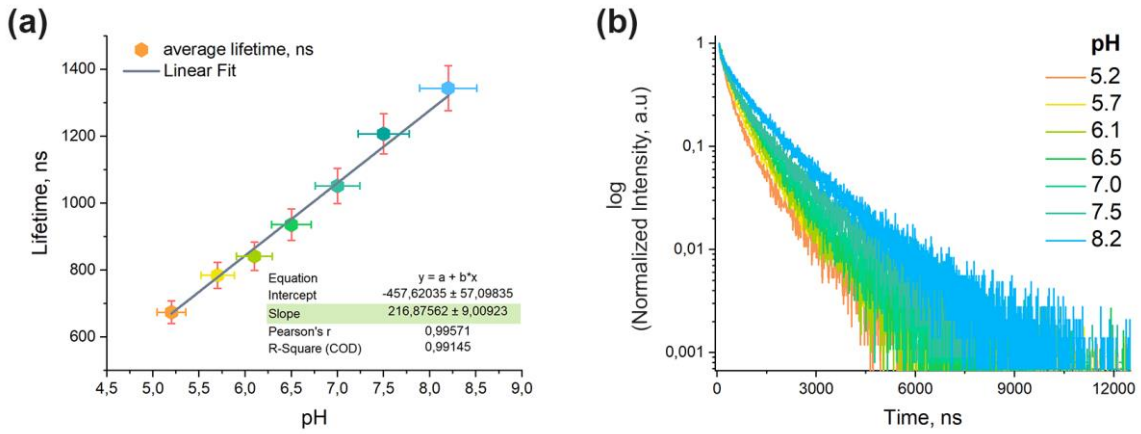

Figure 7. (a) General calibration of **BC-GA-Ir** emission lifetime *vs* pH using pool data obtained in physiological media with averaging for both aerated and degassed solutions; (b) Emission decays in aerated CPB solutions with 9% of DMEM and 1% of FBS at various pH.

These data gave a good linear correlation and uncertainty were calculated as a standard deviation considering the instrumental error of ca. 5% (Figure 7a, Table S27, Supporting Information). To check applicability of this calibration for pH measurements in biosystems, we performed PLIM experiments with Chinese hamster ovary cells (CHO-K1) incubated with **BC-GA-Ir** probe to ensure its suitability for monitoring of intracellular pH, *vide infra*.

2.3. Cell experiments

2.3.1. Cytotoxicity and Localization of Probe in Cells

The cytotoxicity of initial block-copolymers and **BC-GA-Ir** conjugate were evaluated using MTT assay on CHO-K1 cell line upon incubation for 24 h. It was found that the cell viability exceeds 86% for block-copolymer **p(VP-b-VFA)** in the studied range of concentrations from 0.05 to 2 mg/mL, whereas the hydrolysis of the copolymer with formation of primary amino-

groups led to the much higher toxicity: the viability of cells drops lower 50% at the concentrations of **BC-NH$_2$** higher than 0.2 mg/mL (Figure S32, Supporting Information).

When cells are incubated with the cross-linked probe **BC-GA-Ir** cell viability exceeds 75% in the selected range of concentrations that demonstrates acceptable cytotoxicity of the probe and indicates its applicability for bioimaging in living systems.

To investigate the distribution of the probe in subcellular compartments, CHO-K1 cells were co-stained with the **BC-GA-Ir** (0.25 mg/mL) and LysoTracker™ Deep Red (Figure 8_top), LysoTracker™ Green DND-26 (Figure S33), which are organelle-specific probes for acidic compartments (lysosomes and endosomes) and also with BioTracker 405 Blue Mitochondria Dye (Figure 8_bottom) targeted to mitochondria. Z-stack figures of the cells co-stained with LysoTracker™ Deep Red and **BC-GA-Ir** are shown in Figure S34 of the Supporting Information and in Supplied Video.

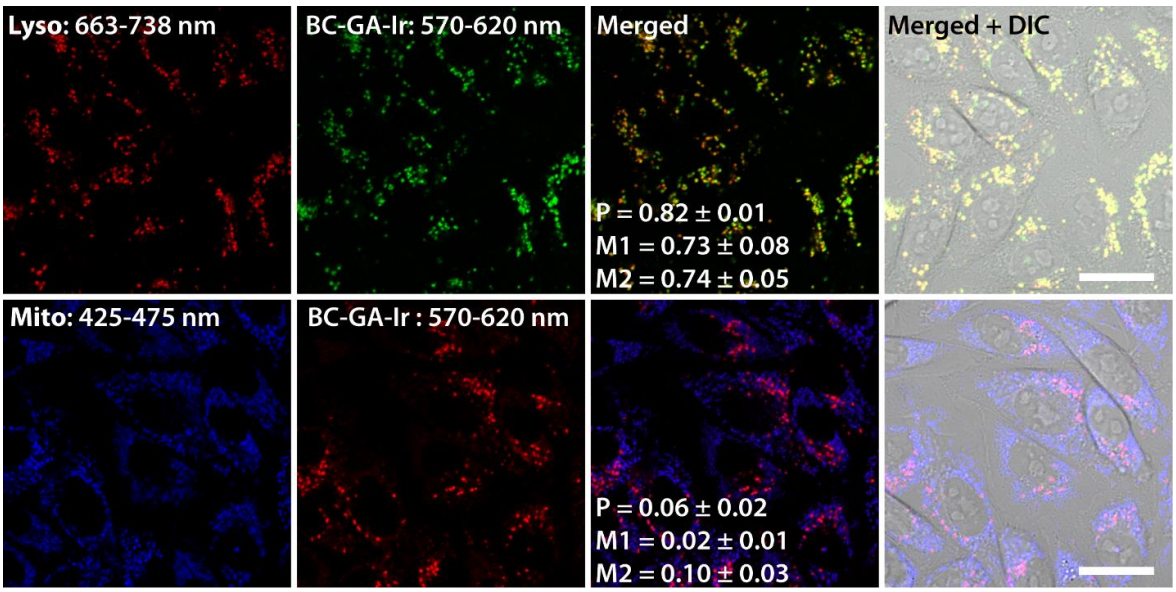

Figure 8. Top: Subcellular distribution of LysoTracker™ Deep Red (red color) and **BC-GA-Ir** (green color) in CHO-K1 cells. Bottom: Subcellular distribution of BioTracker 405 Blue Mitochondria Dye (blue color) and BC-GA-Ir (red color) in CHO-K1 cells. Pearson (P) and Manders overlap coefficients (M1 – fraction of tracker signal that overlaps conjugate signal, M2 – fraction of conjugate signal that overlaps tracker signal) are presented as mean ± standard deviation calculated for 50 cells. Scale bar 20 μm.

Colocalization experiments (Figure 8) clearly indicate that **BC-GA-Ir** displays good membrane permeability and is eventually localized mainly in lysosomes and late endosomes, see the corresponding Pearson and Manders overlap coefficients, Figures 8 and S33 of the Supporting Information. We additionally tested incubation of the probe in presence of

amiloride, which is a well-known inhibitor of macropinosome-mediated endocytosis.[75,76] Figure S35 of Supporting Information shows confocal microscopy of two samples (with and without inhibitor) and the probe emission intensity of cytoplasmic region after 24 hours of incubation averaged for four microphotographs (ca. 50 cells) for each sample. The probe internalizes into cells in both cases, however, the presence of amiloride considerably decreased the uptake. This observation indicates the contribution of micropinocytosis as one of the possible mechanisms of the probe internalization. However, the internalization of BC-GA-Ir may also be realized through other endocytic pathways, which cannot be blocked by amiloride. Thus, the experimental data on application of endocytosis inhibitor (Figure S35 of the Supporting Information) and literature data[77,78] for closely analogous polymeric nanoparticles with the size of ca. 50 nm indicate that endocytic internalization pathway is the most probable mechanism of the probe penetration into cells.

2.3.2. Phosphorescence Lifetime Imaging in Cells

Verification of pH calibration of **BC-GA-Ir** has been done in CHO-K1 cells stained with the probe at concentrations 0.25 and 1 mg/mL for 24 h. To homogenize the intra- and extracellular pH, the cells were additionally incubated for 30-40 min with high K^+ buffers of two different pH (6.0 and 8.0) containing an H^+/K^+ ionophore, nigericin (10 mM).[79] **Figure 9** shows confocal microscopy images, PLIM microphotographs, emission decays and lifetime distributions obtained in this system at pH 6.0 and 8.0 with the probe concentration 0.25 mg/mL. In these experiments, the PLIM signal of **BC-GA-Ir** matches well the confocal images and shows monoexponential decay.

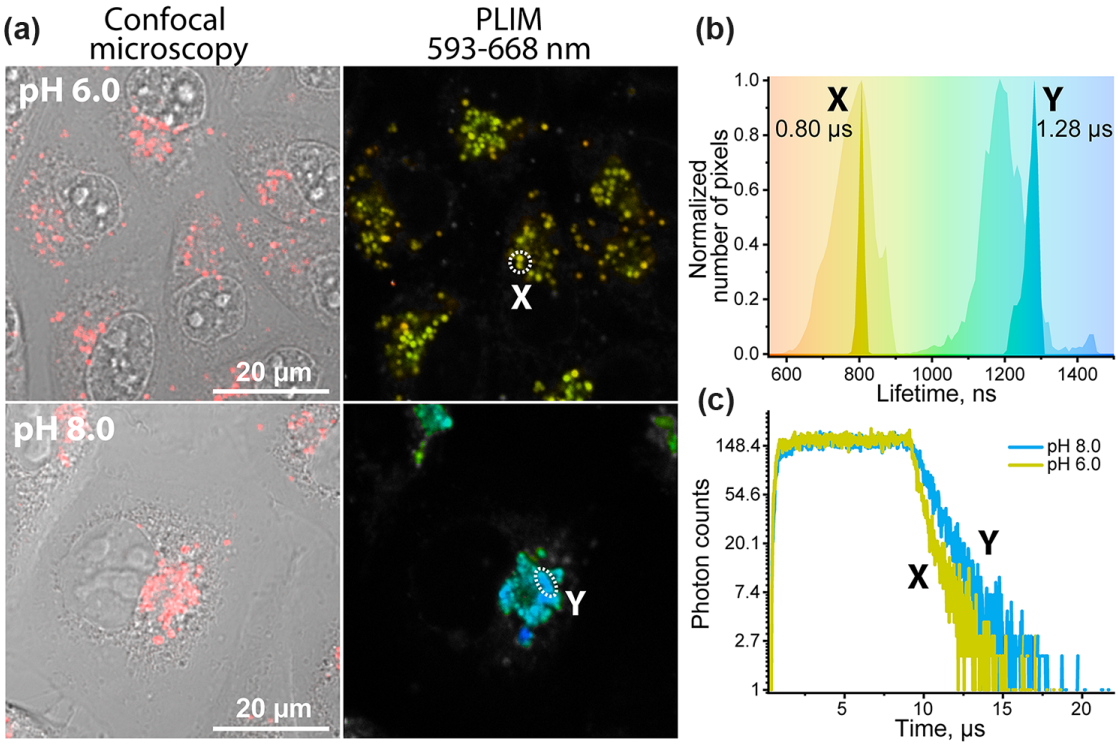

Figure 9. Calibration of **BC-GA-Ir** on living CHO-K1 cells: (a) Confocal images (left; red channel 570-620 nm merged with DIC image) and PLIM images of the same areas (right; color from red to blue denotes lifetime of excited state from 0.57 to 1.50 μs) of cells stained with **BC-GA-Ir** (0.25 mg/mL, 24 h) in nigericin-containing buffers pH 6.0 (top) and 8.0 (bottom); (b) Normalized distributions of excited state lifetime in PLIM experiment at pH 6.0 and 8.0, transparent – the whole image, opaque – selected areas X and Y; (c) Emission decays for selected areas X and Y in PLIM images. Scale bar 20 μm.

We also carried out several repetitions of PLIM after nigericin addition at two different concentration of the probe 0.25 and 1.0 mg/mL (Figure S36, Supporting Information) and analyzed the distribution of lifetime over the whole cells and their brightest spots (Figure 9b,c, S37, 38, Supporting Information). At pH 8.0, the lifetime distribution is rather broad. However, the lifetime of the brightest spots is more uniform and fits well the calibration curve (Figure 9, Figure S38, Supporting Information). On the contrary, the distribution of lifetime at pH 6.0 is sharper and smoother. These findings can be probably explained by intracellular pH homeostasis in the living cell upon induction of media pH well above (8.0) physiologically acceptable interval. Despite the presence of ionophore, the cells tend to maintain the physiological pH in some compartments that results in a rather broad lifetime/pH distribution compared to the PLIM image obtained at pH 6.0. Nevertheless, the average lifetime values of 0.8 and 1.18 μs for pH 6.0 and 8.0, respectively, fits well the pH-calibration curve measured in the model physiological media (Figures 7a, Figure S38, Supporting Information) to give the

magnitudes 5.9 and 7.6 pH units, respectively. These control experiments on living cells in the presence of nigericin showed that the calibration curve built up in solution can be successfully employed for quantitative evaluation of pH in cell samples using **BC-GA-Ir** in PLIM modality.

A study of the dynamics of **BC-GA-Ir** internalization at two concentrations, 0.25 and 1.0 mg/ml, shows that at low concentration, the intensity of the probe emission inside the cells is weak until 24 h of incubation compared to control cells without dye (Figures S39a, S40, Supporting Information), whereas at high concentration, the probe can be detected inside the cell after 1–2 hours of incubation (Figures S39b, S41, Supporting Information). Monitoring of the incubation process in the PLIM mode correlates with luminescent images: after 2 hours of incubation, bright spots are observed inside the cells, the number of which increases significantly over the next 22 hours (Figure 10a).

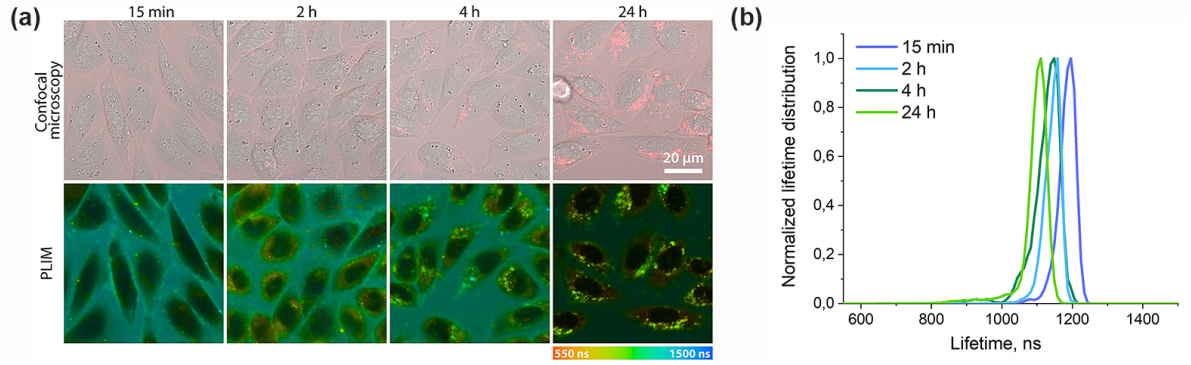

Figure 10. Dynamics of **BC-GA-Ir** (1.0 mg/mL) accumulation by CHO-K1 cells during long-term incubation carried out in DMEM-F12 supplemented with 10% FBS: (a) Confocal images (top; red channel 570-620 nm merged with DIC image) and PLIM images (bottom) of the same areas. (b) Normalized distributions of excited state lifetime of extracellular areas in PLIM experiments. Scale bar 20 µm.

It is important to emphasize that the probe is also detected in the extracellular space both in the images recorded in intensity and in the PLIM modes. Emission lifetime of extracellular area varies during the incubation time from ca. 1200 ns to ca. 1110 ns (Figure 10b). Converting these values to pH using the calibration curve (Figure 7a) gives the values of 7.4 and 7.1, respectively, which can be attributed to slight acidification of the extracellular milieu due to long-term incubation with the probe.

It should be noted that the probe signal after several hours of incubation even at high concentration is still weak to obtain high quality photon statistics in PLIM and we performed further detailed PLIM experiments after incubation for 24 h. CHO-K1 cells incubated with

different concentrations of **BC-GA-Ir** (0.25 mg/mL and 1.00 mg/mL) for 24 h were studied using confocal microscopy together with PLIM (**Figure 11**).

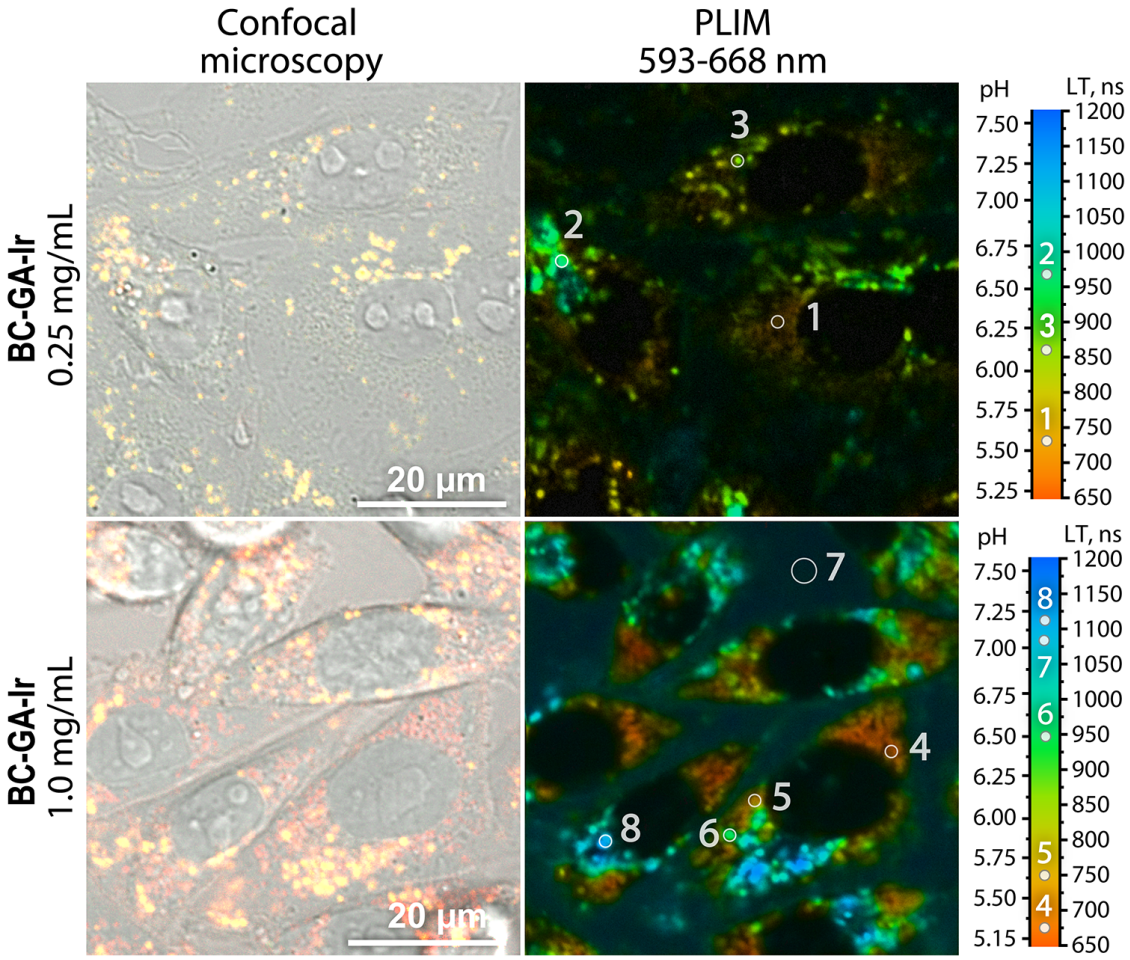

Figure 11. Confocal microscopy (left; merged green channel 500-550 nm, red channel 570-620 nm, and DIC image) and PLIM (right) of living CHO-K1 cells incubated with **BC-GA-Ir** (top: 0.25 mg/mL, bottom: 1.00 mg/mL). In PLIM, the color from red to blue denotes lifetime of excited state from 0.65 to 1.20 μs and corresponding pH from 5.2 to 7.6. Scale bar 20 μm.

The obtained data revealed inhomogeneity of the brightness, color, and lifetime of different possible mechanisms compartments, which is inappreciable at the low concentration of the probe and obvious at higher concentration. Comparison of green (500-550 nm) and red (570-620 nm) channels in the confocal images gives two types of stained compartments: “orange” and “red” (Figure S42, Supporting Information), which also display different lifetimes. Together with the red spectral shift in the “orange” compartments a decrease in the lifetime is also observed. Conversion of the lifetime scale into pH map by means of calibration obtained in the cuvette (Figure 9a) made possible differentiation of intracellular pH in cell compartments. In the “orange” compartments, the lifetime is higher than 850 ns, that is equivalent to pH higher than 6.1 (points 2, 3, 6, 8 on Figure 11). The “red” compartments

show lifetime shorter than 775 ns that corresponds to pH of ca. 5.7 and lower (points 1, 4, 5 on Figure 11). These observations fit well the changes in the emission spectrum of **BC-GA-Ir** found in solution: the red spectral shift of emission band was observed upon solution acidification below pH 5.7 (Figure 7a, Figure S28, Supporting Information).

We also performed several repetitions of PLIM experiment for cells stained with high concentration of the probe. In a few selected cells, we analyzed intercellular areas (dark green color) and intracellular regions marked with different colors corresponding to different lifetime intervals: high lifetime (cyan), middle lifetime (green), low lifetime (orange) (Figure S43a, Supporting Information) and calculated mean values of maxima of lifetime distribution with a confidence interval as mean half-width at half height for those regions. The lifetime data obtained for selected areas were recalculated into pH values by using the calibration curve obtained in solution (Figure 7a, Figure S43b, Supporting Information). These results indicate that in all the tested cells after 24h of incubation extracellular pH remains nearly neutral (mean pH ca. 6.9) while intracellular pH varies from neutral (mean pH ca. 7.0) to slightly acidic (mean pH ca. 6.4) and noticeably acidic (mean pH ca. 5.4). These observations are compatible with the literature data, [80–83] which showed that pH of various compartments formed during the process of endocytosis (early endosomes, recycling endosomes, late endosomes and endosomes fused with lysosomes) varies from 7.0 to 5.5 – 4.2. Therefore, localization of **BC-GA-Ir** in late endosomes and lysosomes is in a good agreement with pH values observed in PLIM experiments described above. Thus, using this probe, the extra- and intracellular pH can be mapped, and endocytic vesicles can be detected and differentiated depending on pH inside the vesicles.

3. Conclusion

A series of phosphorescent $[Ir(N\hat{}C)_2(N\hat{}N)]^+$ complexes containing pH sensitive carboxylic groups in the coordinated ligands have been prepared and characterized. Photophysical properties of the obtained complexes were studied in detail, nature of the emissive transitions was elucidated using DFT and TD DFT calculations. One of these complexes with carboxylated N^C ligands showed reversible protonation/deprotonation equilibria accompanied by clearly visible changes in emission wavelength, intensity, and phosphorescent lifetime, which can be used for pH monitoring in solutions and physiological media. To eliminate a side effect of the sensor phosphorescence quenching by molecular oxygen, this complex was conjugated to water-soluble poly-(vinylpyrrolidone-block-

vinylamine) copolymer, which was additionally cross-linked by glutaraldehyde to prevent oxygen diffusion to the pH sensitive chromophore tightly packed in the polymeric nanoparticles. The calibration of the conjugated probe lifetime *vs* pH displayed strong lifetime dependence on pH and negligible effect of variations in the oxygen concentration in physiologically relevant intervals. However, the calibration showed dependence on the presence of bio-macromolecules (e.g. proteins and components of growing media) that implies obtaining reliable calibration data in the model physiological solutions containing fetal bovine serum and DMEM. Investigation of the probe biological properties using CHO-K1 cell line showed that it has low toxicity, internalizes readily into cells, and is localized mainly in endosomes and lysosomes. PLIM experiments on the cells in the presence of the proton ionophore (nigericin) revealed that the calibration built up for the model physiological media fits well the data obtained in cells that made possible to use the probe for pH mapping in intact living cells. These PLIM data clearly indicate that the probe may be used for quantitative mapping of pH across the sample under study, allow determination of pH gradient in different vesicles and their differentiation from the viewpoint of their acidity.

4. Experimental Section

General experimental details

^{1}H, ^{1}H-^{1}H COSY (400 MHz) NMR spectra were recorded on a Bruker 400 MHz Avance spectrometer, chemical shift values are reported in ppm relative to TMS ($\delta = 0.00$). ^{1}H NMR spectra were calibrated according to the residual signals of methanol-d^4 (3.31 ppm), acetone-d^6 (2.05 ppm), D_2O (4.79 ppm) or DMSO-d^6 (2.50 ppm). Mass spectra were recorded on a Bruker maXis HRMS-ESI-QTOF instrument in positive mode. Elemental analysis was performed using a LECO TruSpec MICRO.

Bis(μ-chlorido) bridged dimeric precursor $\{(N\text{^}C)_2IrCl\}_2$ (N^C = methyl 2-phenylquinoline-4-carboxylate) was synthesized according to published procedures.[42,53–55] 4-(2-(3-Bromophenyl)-1(H)-imidazo [4,5-f] [1,10] phenanthroline-1-yl) benzoic acid (N∧N-Br) was synthesized according to literature methodology.[84] N-vinylpyrrolidone (VP), N-vinylformamide (VFA) (Sigma Aldrich), and dioxane (Vekton) were distilled under vacuum before use. Azobis(isobutyronitrile) (AIBN) was recrystallized two times from ethanol at 60°C and vacuum-dried at 20°C. Trithiocarbonate of the general formula R–S–C(=S)–S–R {dibenzyl carbonotrithioate (R = $–CH_2Ph$) was prepared by the earlier published procedure.[85] Diethyl ether and dimethylsulfoxide (DMSO) (all from Vekton) were used as received. Water

was purified using a “Simplicity” (Merck Millipore) water purification system (type 1 water). DMEM/F12 (Gibco, Carlsbad, CA, USA), Fetal Bovine Serum (Gibco, Carlsbad, CA, USA), penicillin/streptomycin (Thermo Fisher Scientific,Waltham, MA, USA), trypsin-EDTA (Thermo Fisher Scientific, Waltham, MA, USA), MTT reagent 3(4,5-dimethyl-2-thiasolyl)-2,5-diphenyl-2H-tetrasole bromide (Thermo Fisher Scientific, Waltham, MA, USA), DMSO (Merck, Munich, Germany), LysoTracker™ Deep Red (Thermo Fisher Scientific,Waltham, MA, USA), BioTracker 405 Blue Mitochondria Dye (Sigma-Aldrich, Merck, Munich, Germany), Nigericin sodium salt (Sigma-Aldrich) were used as received.

*Synthesis of NN ligand 2,5-dioxopyrrolidin-1-yl-4-(2-(3-bromophenyl)-1H-imidazo[4,5-f][1,10]phenanthrolin-1-yl)benzoate (**N^N-Su**)*

A mixture of 4-(2-(3-bromophenyl) -1(H)-imidazo [4,5-f] [1,10] phenanthroline-1-yl) benzoic acid (100 mg, 0.201 mmol), N,N-dicyclohexylcarbodiimide (41.47 mg, 0.201 mmol), N-hydroxysuccinimide (23.13 mg, 0.201 mmol), and 4-dimethylaminopyridine (5 mg, 0.041 mmol) were stirred in DMF at room temperature for 24 hours. The resulting precipitation was filtered and dissolved in DCM. The solution was placed in a fridge for 30 min and then filtered off in order to remove the precipitates. Finally, the solvent was evaporated, and the product as white solid was washed with diethyl ether (85 mg, Yield: 71%). ^{1}H NMR (400 MHz, DMSO-d_6, δ) 9.12 (dd, *J* = 4.2, 1.6 Hz, 1H), 9.05 (dd, *J* = 8.1, 1.6 Hz, 1H), 9.00 (dd, *J* = 4.2, 1.4 Hz, 1H), 8.42 (d, *J* = 8.4 Hz, 2H), 8.11 (d, *J* = 8.5 Hz, 2H), 7.90 (dd, *J* = 8.1, 4.3 Hz, 1H), 7.86 (s, 1H), 7.64 (d, *J* = 8.0 Hz, 1H), 7.60 (dd, *J* = 8.5, 4.3 Hz, 1H), 7.51 (dd, *J* = 8.4, 1.3 Hz, 1H), 7.43 (d, *J* = 7.9 Hz, 1H), 7.37 (t, *J* = 7.8 Hz, 1H), 2.96 (s, 4H). HRMS (ESI) *m/z*: $[M+H]^+$ calcd for C30H19BrN5O4, 594.0601; found, 594.0595; $[M+Na]^+$ calcd for $C_{30}H_{19}BrN_5O_4Na$, 616.0421; found, 616.0418.

Synthesis of iridium(III) complexes

*$[(N^C)_2Ir(N^N\text{-}Br)\text{-}COOH]ClO_4$ (**Ir-OMe**).*

The corresponding bis(μ-chlorido)bridged dimeric precursor (55,6 mg, 0,037 mmol) was suspended in DCM/MeOH 1:1 mixture (5 ml) and solution of NN(Br)-COOH (37,2 mg, 0,075 mmol) in 5 ml of the same solvent was added. The reaction mixture was heated at 40^{o}C for 3 h. The resulting clear red solution was cooled to room temperature, excess of solid $KClO_4$ was added and the mixture was stirred for 30 minutes. The obtained reaction mixture was evaporated to dryness, dissolved in DCM, filtered off and evaporated again. The crude product was purified by flash column chromatography (eluent DCM:MeOH 5:1) and after evaporation the final product was obtained as red solid (98 mg,) ^{1}H NMR (400 MHz,

Methanol-d_4, δ) 9.20 (dd, *J* = 8.3, 1.1 Hz, 1H), 8.84 (s, 1H), 8.79 (s, 1H), 8.71 – 8.61 (m, 1H), 8.59 – 8.48 (m, 1H), 8.41 (t, *J* = 7.6 Hz, 2H), 8.35 – 8.17 (m, 4H), 8.06 (dd, *J* = 8.3, 5.2 Hz, 1H), 7.76 (t, *J* = 1.6 Hz, 1H), 7.70 (dd, *J* = 8.2, 1.7 Hz, 1H), 7.67 – 7.58 (m, 3H), 7.58 – 7.49 (m, 2H), 7.46 (d, *J* = 8.9 Hz, 1H), 7.38 (d, *J* = 7.9 Hz, 1H), 7.31 (t, *J* = 7.7 Hz, 2H), 7.24 (dd, *J* = 12.8, 5.4 Hz, 1H), 7.19 (d, *J* = 8.0 Hz, 1H), 7.02 – 6.79 (m, 4H), 6.68 (dd, *J* = 7.4, 4.1 Hz, 2H). HRMS (ESI) *m/z*: $[M]^+$ calcd for $C_{60}H_{39}BrIrN_6O_6$, 1211.1726; found, 1211.1758. Anal. calcd for $C_{60}H_{39}BrClIrN_6O_{10}$: C, 54.95; H, 3.00; N, 6.41; Found: C, 54.88; H, 3.08; N, 6.35.

*$Na_2[(N^C\text{-}COO)_2Ir^+(N^N\text{-}Br)\text{-}COO^-)]$ (**Ir-ONa**)*

Methanol solution (10 mL) of **Ir-OMe** (17.9 mg, 0.015 mmol) were placed in a round-bottom flask and 8.3 mg (0.06 mmol) of Na_2CO_3 were added. The reaction mixture was heated at 40ºC for ca. 4 hours and evaporated to dryness. The crude product was dissolved in 1 mL of MeOH and 5mL of acetone was added to precipitate NaOTf and unreacted Na_2CO_3. The resulting orange solution was filtered and evaporated to give orange solid.

^{1}H NMR (400 MHz, Methanol-d_4, δ) 9.20 (dd, *J* = 8.3, 1.3 Hz, 1H), 8.67 (dd, *J* = 5.2, 1.3 Hz, 1H), 8.57 – 8.50 (m, 1H), 8.42 (s, 1H), 8.38 (s, 1H), 8.28 – 8.16 (m, 4H), 8.12 (dd, *J* = 8.3, 1.1 Hz, 1H), 8.04 (dd, *J* = 8.3, 5.2 Hz, 1H), 7.84 (t, *J* = 1.7 Hz, 1H), 7.67 – 7.52 (m, 5H), 7.44 (d, *J* = 8.1 Hz, 1H), 7.38 (d, *J* = 8.9 Hz, 1H), 7.33 (d, *J* = 8.9 Hz, 1H), 7.28 – 7.15 (m, 5H), 6.91 – 6.73 (m, 4H), 6.66 (dd, *J* = 7.0, 5.3 Hz, 2H). HRMS (ESI) *m/z*: $[M]^-$ calcd for $C_{58}H_{33}BrIrN_6O_6$, 11811.1266; found, 1181,1303. Anal. calcd for $C_{58}H_{32}BrIrN_6Na_2O_6$: C, 56.77; H, 2.63; N, 6.85; Found: C, 56.94; H, 2.83; N, 6.95.

*$[(N^C)_2Ir(N^N(Br)\text{-}Su)]OTf$ (**Ir-Su**).*

The corresponding dimeric precursor was converted at first to labile bis(acetonitrile) complex by the reaction with AgOTf in acetonitrile. Resulting $[(CN)_2Ir(NCMe)_2]OTf$ complex (81 mg, 0.084 mmol) was dissolved in 5 mL of DCM followed by the addition of **NN-Su** ligand (50 mg, 0.084 mmol) DCM solution (5 mL).

^{1}H NMR (400 MHz, Methanol-d_4, δ) 9.23 (d, *J* = 8.2 Hz, 1H), 8.85 (s, 1H), 8.80 (s, 1H), 8.67 (dd, *J* = 5.1, 1.2 Hz, 1H), 8.59 – 8.51 (m, 1H), 8.48 – 8.39 (m, 3H), 8.37 (d, *J* = 10.2 Hz, 1H), 8.33 (d, *J* = 7.9 Hz, 1H), 8.29 (d, *J* = 7.8 Hz, 1H), 8.08 (dd, *J* = 8.3, 5.2 Hz, 1H), 7.86 (dd, *J* = 8.3, 1.9 Hz, 1H), 7.84 – 7.82 (m, 1H), 7.80 (dd, *J* = 8.3, 1.9 Hz, 1H), 7.70 (d, *J* = 3.6 Hz, 2H), 7.59 (d, *J* = 8.0 Hz, 1H), 7.53 (d, *J* = 8.9 Hz, 1H), 7.47 (d, *J* = 8.9 Hz, 1H), 7.38 – 7.20 (m, 6H), 6.98 – 6.83 (m, 4H), 6.69 (dd, *J* = 7.2, 5.4 Hz, 2H), 4.13 (s, 3H), 4.11 (s, 3H), 2.96 (s, 4H). HRMS (ESI) *m/z*: $[M]^+$ calcd for C64H42BrIrN7O8, 1308.1891; found, 1308.1910.

Synthesis of polymers and conjugates

*Synthesis of **p(VP)***

Macro-RAFT agent was synthesized via thermally initiated polymerization of VP in bulk at 80°C for 24 hours. The sample for VP (37 mmol) polymerization was prepared by dissolving a chain transfer agent (CTA), S,S- dibenzyltrithiocarbonate, (10^{-2} M) and AIBN (10^{-3} M) in the monomer.[86] The solution was placed in a Pyrex reactor, degassed by three repeated freeze−evacuate−thaw cycles and sealed. The obtained polymer was purified by triple recrystallization and centrifugation from diethyl ether. The yield equaled ca. 50 %.^{1}H NMR (400 MHz, Water-d_2, δ) 3.97 – 3.42 (m, 1H), 3.42 – 2.86 (m, 2H), 2.61 – 2.16 (m, 2H), 2.16 – 1.87 (m, 2H), 1.87 – 1.34 (m, 2H).

*Synthesis of **p(VP-b-VFA)***

Block-copolymer was prepared by copolymerization of VFA (1.5 mmol) and Macro-RAFT VP agent (200 mg) at 80°C for 30 hours. Both reagents were dissolved in dioxane (4 ml) and placed into a Pyrex reactor. AIBN (10^{-3} M) was then added and the solution was degassed by three repeated freeze−evacuate−thaw cycles and sealed. The final block-copolymer p(VP-b-VFA) was purified by dialysis (Orange Scientific; molecular weight cutoff = 6−8 kDa) for 3 days to remove the residual monomers and solvent and isolated from water by freeze-drying (FreeZone, Labconco). The yield was ca. 42 %. ^{1}H NMR (400 MHz, Water-d_2, δ) 8.32 – 7.52 (m, 0.2H), 3.97 – 3.42 (m, 1.2H), 3.42 – 2.86 (m, 2H), 2.61 – 2.16 (m, 2H), 2.16 – 1.87 (m, 2H), 1.87 – 1.34 (m, 2.4H).

*Block-Copolymer Hydrolysis (**BC-NH$_2$**)*

Hydrolysis of formamide groups of the VFA-units to primary amino groups was carried out in 8.5% hydrochloric acid at 60˚C during 24 hours. The degree of hydrolysis was estimated by ^{1}H NMR (400 MHz, Water-d_2, δ) 3.97 – 3.42 (m, 1.2H), 3.42 – 2.86 (m, 2H), 2.61 – 2.16 (m, 2H), 2.16 – 1.87 (m, 2H), 1.87 – 1.34 (m, 2.4H).

*Conjugation of Block-Copolymer and Iridium Complex (**BC-Ir**)*

Covalent conjugation of iridium complex to the block-copolymer was performed by the reaction of VA amino groups of the copolymer and N-hydroxysuccinimidyl function of **Ir-Su**. Typically, block-copolymer p(VP-VA) (25 mg) was first dissolved in methanol under stirring. **Ir-Su** (0.15 mg) was also dissolved in methanol and then added to the solution of the copolymer. The reaction was left for overnight at room temperature in the presence of a drop of triethylamine. Na_2CO_3 was then added to the mixture to increase pH, and the temperature

was raised to 50˚C to start the hydrolysis of ester groups of iridium complex. The reaction was controlled visually by changing the color from red to orange. The conjugate was purified by dialysis and freeze-dried.

*Cross-linking of conjugate (**BC-GA-Ir**)*

The final stage of preparation is cross-linking of the conjugates by interaction of the unreacted primary amino groups with glutaraldehyde (GA). The conjugate **BC-Ir** (25 mg) was dissolved in PBS with pH=7.4, GA (2 µmol) was then added to the solution and the reaction mixture was stirred for 4 hours at room temperature followed by addition of glycine (0.1 mmol) sodium borohydride 0.5% (wt./vol.) to mask unreacted aldehyde groups. The final compound was also purified by dialysis and freeze-dried.

Characterization of Block-Copolymer and Its Conjugate with iridium Complex

Molecular weights (MW) of block-copolymers were estimated by analytical gel permeation chromatography (GPC) on "Prominence 20" chromatograph (Shimadzu) using the TSKgel SuperAW4000 column. The samples were dissolved in acetonitrile/0.1 M NaCl (20/80 vol.%). Chromatography was carried out at 20 °C with sample aliquot of 20 µl and eluent flow rate of 0.5 ml/min. Hydrodynamic diameters and ζ-potentials (in 10^{-3} M NaCl) on dependence on pH were determined by Malvern ZetaSizer NanoZS.

Photophysical experiments

All photophysical measurements were carried out in freshly distilled methanol or in water (type 1, purified with Merck Millipore system). A Shimadzu UV-1800 spectrophotometer and a Fluorolog-3 (JY Horiba Inc.) spectrofluorimeter were used to record the UV/Vis and excitation spectra, respectively. Emission spectra in solution were measured using a DTL–375QT pulse laser (wavelength 355 nm, pulse width 5 ns, repetition frequency 10 −1000 Hz), an Ocean Optics monochromator (Monoscan-2000, interval of wavelengths 1 nm), a FASTComTec (MCS6A1T4) multiple-event time digitizer. A Hamamatsu (H10682-01) photon counting head were used for lifetime measurements. The absolute emission quantum yield in solution was determined by a comparative method using LED 365 nm pumping and $Ru(bipy)_3Cl_2$ in aerated aqueous solution ($\Phi_r = 0.04$)[87] as the reference with the refraction coefficients of methanol and water are equal to 1.34 and 1.33, respectively. The following equation

$$\Phi_s = \Phi_r \frac{\eta_s^2 A_r I_s}{\eta_r^2 A_s I_r}$$

was used to calculate the quantum yield, where Φ_s is the quantum yield of the sample, Φ_r is the quantum yield of the reference, η is the refractive index of the solvent, A_s and A_r are the absorbance of the sample and the reference at the wavelength of excitation, respectively, I_s and I_r are the integrated areas of emission bands. The lifetime data fit has been done using the OriginPro®2021 software package.

The pKa of **Ir-OH/ONa** and **BC-GA-Ir** were calculated according to the according to the modified equation [88,89]

$$pKa = pH - log\frac{\tau_x - \tau_a}{\tau_b - \tau_x}$$

where τ_x, - the emission lifetimes at a defined pH within the titration plot, τ_a – lifetime of the acid form, τ_b - lifetime of the base form.

The linear fit of the pH dependence *vs* $\log[(\tau_x-\tau_a)/(\tau_b-\tau_x)]$ makes possible pKa calculation.[88,89]

All measurements of the lifetimes in aqueous solutions for polymeric conjugates were carried out at 310 K. Phosphate buffer, Phosphate buffered saline, citrate buffer or Citrate-Phosphate buffer was used to control the pH of the samples. pH values were determined using a pH-meter («Expert pH», Econic-Expert) with a laboratory combined pH electrode ESK-10601/7). Buffer solutions with 0.1 N NaCl and 0.001 M Ca^{2+}, Mg^{2+} were used to determine the effect of salinity and cations on the lifetime response.

Two series of solutions with different amounts of DMEM and FBS were prepared. **Series 1.** A solution of **BC-GA-Ir** (5 mg/mL, 500 μL) was added to 4 mL of corresponding Citrate-Phosphate Buffer solution, then 450 μL of DMEM and 50 μL of FBS was added (for a final amount of DMEM – 9%, FBS – 1%). The final pH values were determined using a pH meter and adjusted to the desired pH if necessary. Two independent solutions were prepared with **BC-GA-Ir** from different syntheses. **Series 2.** A solution of **BC-GA-Ir** (5 mg/mL, 50 μL) was added to 2.4 mL of PBS, then 40 μL of FBS was added (for a final amount of about 15%). The resulting solutions were adjusted to the required pH values with citric acid or NaOH.

The lifetime data were fit using the Origin 9.0 program. The intensity-weighted average lifetimes for biexponential decay were calculated using the equation:

$$\tau_{av} = \frac{A_1\tau_1^2+A_2\tau_2^2}{A_1\tau_1+A_2\tau_2},$$

where A_i is the weight of the i-exponent and τ_i is the corresponding lifetime component.

The obtained six sets of data from the **Series 1** and **2** were used for calculating their variance using the formula:

$$Sd(y) = \frac{1}{n}\sum_{i=1}^{n}|y_i - \bar{y}|,$$

were n – number of experiments, y_i – lifetime value in i_{th} experiment, $\bar{y}$ - the average value of the lifetime in all experiments.

The instrumental uncertainty of lifetime measurements is ca. 5%, which proved to be higher than any of the variances obtained upon averaging of experimental data (Table S26). We used this value to show standard deviation at ordinate axis (Figure 7a). The standard deviation at the abscissa (pH) axis was calculated from a linear fit of the data using the appropriate slope factor.

Computational Details

The quantum chemical calculation of the Ir complexes depending on pH was performed using the Gaussian 16 software package[90] in the DFT methodology. MN12SX functional[91] was chosen with the 6-311+G* basis set on heteroatoms, 6-31G* for C and H and Stuttgart/Dresden effective core potential[92] on Ir, which demonstrated a good reproducibility of experimental data in our previous work.[93] The solvent methanol was applied in the PCM model.[94] The geometries of the triplet states were optimized using TD DFT.[95] To obtain natural transition orbitals (NTO)[96] and interfragment charge transfer (IFCT) tables the Multiwfn program was employed.[97]

The electronic density difference, EDD (Δρ), between excited T_i and ground states S_0 was evaluated as the difference between squares of HOMO and LUMO NTOs:

$$\Delta\rho(T_i \rightarrow S_0) = \sum_k|\psi_{ik}(occ)|^2 - \sum_k|\psi_{ik}(virt)|^2.$$

Cell experiments

Cell Culturing

The Chinese hamster ovary cells (CHO-K1) were cultured in DMEM/F12 medium supplemented with FBS (10 vol. %), glutamine (2 mM), and penicillin/streptomycin (100 U/mL). Cell cultures were maintained in a humidified incubator with 5% CO2 at 37°C, and passaged routinely using trypsin-EDTA. For living-cell confocal microscopy, the cells (1×10^5 CHO-K1 cells in 1.5 mL growing media) were seeded in glass-bottom 35 mm dishes (Ibidi GmbH, Gräfelfing, Germany) and incubated for 48 h until reaching a confluence of ca. 70%. Phosphorescent probe **BC-GA-Ir** was dissolved in growing media at a concentration of

4 mg/mL, passed through a syringe filter with a pore size of 0.2 µm, and added to the cells at a final concentration of 0.3–1 mg/mL. After incubation with the probe for 24 h, cells were washed with fresh media with all supplements and used for microscopy.

MTT Assay

CHO-K1 cells were seeded in 96-well flat-bottom plates (TPP Techno Plastic Products AG, Trasadingen, Switzerland) 1×10^4 cells in 100 µL of culture medium per well and incubated at 37°C under 5% CO_2 for 24 h. **BC-NH2**, **p(Vp-b-VFA)**, and **BC-GA-Ir** were then added to the cells at concentrations of 0.05–2 mg/mL. After incubation for 24 h, the cells were subsequently treated with MTT reagent, 3(4,5-dimethyl-2-thiasolyl)-2,5-diphenyl-2H-tetrasole bromide, at the concentration of 0.5 mg/mL. After further incubation for 2 h, the media was removed, and the formazan crystals were dissolved in DMSO (100 µL/well) at 37°C for 15 min. Using a SPECTROstar Nano microplate reader (BMG LABTECH, Ortenberg, Germany), the absorbance at 570 nm was measured in each well. Viability was determined as a ratio of the average absorbance value of the wells containing probes to that of the control wells. The results are shown as mean ± standard deviation of 6 repetitions.

Organelles vital Staining

LysoTracker™ Deep Red, LysoTracker™ Green DND-26 were used for the vital staining of lysosomes and late endosomes in CHO-K1 cells, BioTracker 405 Blue Mitochondria Dye was used for the vital staining of mitochondria. Cells were incubated with BC-GA-Ir 0.25 mg/ml for 24 h, washed with fresh media 3 × 1 mL and then incubated with a new portion of growing media for 15 min. The dyes were added to the cells at the concentration of 50 nM and cells were further incubated for 15 (for mitochondria dye) and 30 (for lysosomal dye) minutes prior to confocal microscopy.

Macropinocytosis assay

5-(N,N-Hexamethylene)amiloride (Sigma-Aldrich, Merck) was dissolved in DMSO to obtain the solution with the concentration of 100 mM, which was then added to 1 mL of DMEM/F12 giving the final inhibitor concentration of 66 µM. The CHO-K1 cells were incubated with this solution for 1 h at 37 °C and 5% CO2 atmosphere. Then the media was replaced with the fresh supplemented growing media containing **BC-GA-Ir** (1.00 mg/mL). In parallel, a control sample without amiloride was prepared analogously. The both samples were incubated with the probe for 24 h at 37 °C and 5% CO2 atmosphere prior to confocal microscopy. Because amiloride is strongly luminescent under excitation at 405 nm the microscopic experiment was

performed with the excitation at 487 nm and emission of the probe was recorded in the red channel (570-620 nm).

Intracellular pH calibration

The CHO-K1 cells seeded in glass-bottom 35 mm dishes were incubated with **BC-GA-Ir** (0.25 mg/mL) at 37 °C for 24 h. To maintain a specific pH, high K^+ buffer (30 mM NaCl, 120 mM KCl, 1 mM $CaCl_2$, 0.5 mM $MgSO_4$, 1 mM KH_2PO_4, 5 mM glucose, 20 mM HEPES) with various in pH values (6.0 and 8.0) was used.[98–100] The cells were washed with the buffer 4 × 1 mL and then incubated in the buffer in presence of nigericin (10 μM) at 37 °C for 30-40 min prior to confocal microscopy.

Confocal Luminescence Microscopy and PLIM Experiment

All measurements were performed in humidified Stage Top Incubator Tokai HIT (Fujinomiya, Japan) at 37°C. Imaging of living CHO-K1 cells was carried out by using a confocal inverted Nikon Eclipse Ti2 microscope (Nikon Corporation, Tokyo, Japan) with 60× oil immersion objective. The emission of BC-GA-Ir was excited with 405 nm laser and recorded in 500–550 nm (green channel) or 570–620 nm (red channel) ranges. The fluorescence of LysoTracker™ Deep Red was excited at 638 nm and recorded at 663–738 nm. The fluorescence of LysoTracker™ Green DND-26 was excited at 405 nm and recorded at 500–550 nm (green channel). The fluorescence of BioTracker 405 Blue Mitochondria Dye was excited at 405 nm and recorded at 425–475 nm (blue channel). Luminescent confocal microphotographs were complemented with differential interference contrast (DIC) images. The images were processed and analyzed using ImageJ software (National Institutes of Health, Bethesda, MY, USA). The quantitative co-localization analysis was performed using ImageJ JACoP Plugin to determine Pearson (P) and Manders (M1, M2) co-localization coefficients. Thresholds for M1 and M2 calculation were set by a visually estimated value for each channel. Results are represented as mean ±standard deviation.

Phosphorescence lifetime imaging microscopy (PLIM) of CHO-K1 cells was carried out using a time-correlated single-photon counting (TCSPC) DCS-120 module (Becker&Hickl GmbH, Berlin, Germany) integrated into the Nikon Eclipse Ti2 confocal instrument. Emission was excited with a picosecond laser at 405 nm, phosphorescence was recorded using 575 nm long pass filter and 630/75 nm band pass filter and pinhole of 0.5–1.5. The following settings were used: frame time 7.30 s, pixel dwell time 27.30 μs, points number 1024, time per point 25.00 ns, time range of PLIM recording 25.60 μs, total acquisition time 100–140 s, and image size 512×512 pixels. Oil immersion 60× objective with zoom 5.33

provided a scan area of 0.05 mm × 0.05 mm. Phosphorescence lifetime data were processed with SPCImage 8.1 software (Becker & Hickl GmbH, Berlin, Germany) using monoexponential decay modes with an average goodness of the fit $0.8 \leq \chi^2 \leq 1.2$. The average number of photons per curve were not less than 2500 at binning 7–8. The colors in the PLIM images show the measured lifetimes.

Supporting Information

Supporting Information is available from the Wiley Online Library or from the author.

Acknowledgements

The authors acknowledge the financial support from Russian Science Foundation (grant 19-13-00132-П). The experimental studies were carried out using equipment of the Research Park of St. Petersburg State University (Centers for Magnetic Resonance, for Optical and Laser Materials Research, for Chemical Analysis and Materials Research, and Computing Centre). The authors are also grateful Prof. Sivtcov and A. Gostev from St.Petersburg State Institute of Technology for providing the RAFT agent. The authors are grateful to Dr. Elena S. Kornilova (Institute of Cytology, Russian Academy of Sciences) and her colleagues for valuable advice on the study of endocytosis and for the kindly provided amiloride.

References

[1] K. Teter, G. Chandy, B. Quiñones, K. Pereyra, T. Machen, H.-P. H. Moore, *Journal of Biol. Chem.***1998**, *273*, 19625.

[2] D. J. Yamashiro, B. Tycko, S. R. Fluss, F. R. Maxfield, *Cell* **1984**, *37*, 789.

[3] D. Neri, C. T. Supuran, *Nat. Rev. Drug Discov.* **2011**, *10*, 767.

[4] B. A. Webb, M. Chimenti, M. P. Jacobson, D. L. Barber, *Nat. Rev. Cancer* **2011**, *11*, 671.

[5] D. Lagadic-Gossmann, L. Huc, V. Lecureur, *Cell Death Differ.* **2004**, *11*, 953.

[6] S. Simon, D. Roy, M. Schindler, *P. Natl. Acad. Sci. USA* **1994**, *91*, 1128.

[7] I. L. Medintz, M. H. Stewart, S. A. Trammell, K. Susumu, J. B. Delehanty, B. C. Mei, J. S. Melinger, J. B. Blanco-Canosa, P. E. Dawson, H. Mattoussi, *Nat. Mater.* **2010**, *9*, 676.

[8] S. Singha, D. Kim, H. Seo, S. W. Cho, K. H. Ahn, *Chem. Soc. Rev.* **2015**, *44*, 4367.

[9] X. Li, X. Gao, W. Shi, H. Ma, *Chem. Rev.* **2014**, *114*, 590.

[10] M. Gao, F. Yu, C. Lv, J. Choo, L. Chen, *Chem. Soc. Rev.* **2017**, *46*, 2237.

[11] A. Steinegger, O. S. Wolfbeis, S. M. Borisov, *Chem. Rev.* **2020**, *120*, 12357.

[12] D. Aigner, S. M. Borisov, P. Petritsch, I. Klimant, *Chem. Comm.* **2013**, *49*, 2139.

[13] D. Aigner, B. Ungerböck, T. Mayr, R. Saf, I. Klimant, S. M. Borisov, *J. Mater. Chem. C* **2013**, *1*, 5685.

[14] M. J. Hall, L. T. Allen, D. F. O'Shea, *Org. Biomol. Chem.* **2006**, *4*, 776.

[15] A. Méndez-Ardoy, J. J. Reina, J. Montenegro, *Chem. – Eur. J.* **2020**, *26*, 7516.

[16] S. Wu, H. Min, W. Shi, P. Cheng, *Adv. Mater.* **2020**, *32*, 1805871.

[17] J. Han, K. Burgess, *Chem. Rev.***2010**, *110*, 2709.

[18] V. I. Martynov, A. A. Pakhomov, I. E. Deyev, A. G. Petrenko, *BBA – Gen. Subjects* **2018**, *1862*, 2924.

[19] R. P. Haugland, *The Handbook: A Guide to Fluorescent Probes and Labeling Technologies*, Molecular Probes (Invitrogen), Carlsbad, CA, USA, **2005**.

[20] Wolfgang Becker, *Advanced Time-Correlated Single Photon Counting Applications* (Ed.: Becker, W.), Vol. 111, Springer International Publishing, Cham, **2015**.

[21] R. Datta, T. M. Heaster, J. T. Sharick, A. A. Gillette, M. C. Skala, *J. Biomed. Opt.* **2020**, *25*, 071203.

[22] T. Nakabayashi, N. Ohta, *Anal.Sci.* **2015**, *31*, 275.

[23] R. N. Day, N. Mazumder, Y. Sun, K. G. Christopher, *Springer Series Chem.* **2015**, *111*, 249.

[24] D. Aigner, R. I. Dmitriev, S. M. Borisov, D. B. Papkovsky, I. Klimant, *J. Mater. Chem. B* **2014**, *2*, 6792.

[25] P. J. Pacheco-Liñán, M. Moral, M. L. Nueda, R. Cruz-Sánchez, J. Fernández-Sainz, A. Garzón-Ruiz, I. Bravo, M. Melguizo, J. Laborda, J. Albaladejo, *J. Phys. Chem. C* **2017**, *121*, 24786.

[26] N. Marcotte, A. M. Brouwer, *J. Phys. Chem. B* **2005**, *109*, 11819.

[27] A. S. Goryashchenko, A. A. Pakhomov, A. v. Ryabova, I. D. Romanishkin, E. G. Maksimov, A. N. Orsa, O. v. Serova, A. A. Mozhaev, M. A. Maksimova, V. I. Martynov, A. G. Petrenko, I. E. Deyev, *Biosensors* **2021**, *11*, 340.

[28] M. V. Shirmanova, T. F. Sergeeva, A. I. Gavrina, V. V. Dudenkova, K. A. Lukyanov, E. V. Zagaynova, *Proc. SPIE 10498, Multiphoton Microscopy in the Biomedical Sciences XVIII*, **2018**, 1049807.

[29] S. Kumar, S. Singh, A. Kumar, K. S. R. Murthy, A. Kumar Singh, *Coord. Chem. Rev.* **2022**, *452*, 214272.

[30] M. Rajendran, B. Claywell, E. P. Haynes, U. Scales, C. K. Henning, M. Tantama, *ACS Omega* **2018**, *3*, 9476.

[31] P. S. Chelushkin, J. R. Shakirova, I. S. Kritchenkov, V. A. Baigildin, S. P. Tunik, *Dalton Trans.* **2022**, *51*, 1257.

[32] K. Y. Zhang, Q. Yu, H. Wei, S. Liu, Q. Zhao, W. Huang, *Chem. Rev.* **2018**, *118*, 1770.

[33] M. H. Y. Cheng, Y. Mo, G. Zheng, *Adv. Healthc. Mater.* **2021**, *10*, 2001549.

[34] S. Prasad, A. Chandra, M. Cavo, E. Parasido, S. Fricke, Y. Lee, E. D'Amone, G. Gigli, C. Albanese, O. Rodriguez, L. L. del Mercato, *Nanotechnology* **2021**, *32*, 062001.

[35] P. Y. Ho, C. L. Ho, W. Y. Wong, *Coord. Chem. Rev.* **2020**, *413*, 213267.

[36] R. I. Dmitriev, D. B. Papkovsky, *Methods Appl. Fluoresc.* **2015**, *3*, 034001.

[37] D. B. Papkovsky, R. I. Dmitriev, *Cell Mol. Life Sci.* **2018**, *75*, 2963.

[38] Z. Chen, X. Meng, M. Xie, Y. Shi, L. Zou, S. Guo, J. Jiang, S. Liu, Q. Zhao, *J. Mater. Chem. C* **2020**, *8*, 2265.

[39] J. B. Liu, K. Vellaisamy, G. Li, C. Yang, S. Y. Wong, C. H. Leung, S. Z. Pu, D. L. Ma, *J. Mater. Chem. B* **2018**, *6*, 3855.

[40] D. C. Goldstein, Y. Y. Cheng, T. W. Schmidt, M. Bhadbhade, P. Thordarson, *Dalton Trans.* **2011**, *40*, 2053.

[41] H. Chen, C. Ge, H. Cao, X. Zhang, L. Zhang, L. Jiang, P. Zhang, Q. Zhang, *Dalton Trans.* **2019**, *48*, 17200.

[42] J. Weng, Q. Mei, W. Jiang, Q. Fan, B. Tong, Q. Ling, W. Huang, *Analyst* **2013**, *138*, 1689.

[43] R. T. Brown, N. C. Fletcher, L. Danos, N. R. Halcovitch, *Eur. J. Inorg. Chem.* **2019**, *2019*, 110.

[44] P. Pal, T. Ganguly, S. Das, S. Baitalik, *Dalton Trans.* **2021**, *50*, 186.

[45] Y. Ma, H. Liang, Y. Zeng, H. Yang, C. L. Ho, W. Xu, Q. Zhao, W. Huang, W. Y. Wong, *Chem. Sci.* **2016**, *7*, 3338.

[46] P. Yang, S. Zhang, K. Wang, H. Qi, *Dalton Trans.* **2021**, *50*, 17338.

[47] S. Moromizato, Y. Hisamatsu, T. Suzuki, Y. Matsuo, R. Abe, S. Aoki, *Inorg. Chem.* **2012**, *51*, 12697.

[48] K. Qiu, L. Ke, X. Zhang, Y. Liu, T. W. Rees, L. Ji, J. Diao, H. Chao, *Chem. Comm.* **2018**, *54*, 2421.

[49] R. J. Meier, J. M. B. Simbürger, T. Soukka, M. Schäferling, *Chem. Comm.* **2015**, *51*, 6145.

[50] C. Wei, H. Wei, W. Yan, Z. Zhao, Z. Cai, B. Sun, Z. Meng, Z. Liu, Z. Bian, C. Huang, *Inorg. Chem.* **2016**, *55*, 10645.

[51] K. Gupta, M. Verma, P. Srivastava, S. Sivakumar, A. K. Patra, *New J. Chem.* **2020**, *44*, 3570.

[52] X. Zhang, Y. Jiao, X. Jing, H. Wu, G. He, C. Duan, *Dalton Trans.* **2011**, *40*, 2522.

[53] J. R. Shakirova, O. A. Tomashenko, E. E. Galenko, A. F. Khlebnikov, P. Hirva, G. L. Starova, S. H. Su, P. T. Chou, S. P. Tunik, *Inorg. Chem.* **2018**, *57*, 6853.

[54] C. Huang, G. Ran, Y. Zhao, C. Wang, Q. Song, *Dalton Trans.* **2018**, *47*, 2330.

[55] R. A. Smith, E. C. Stokes, E. E. Langdon-Jones, J. A. Platts, B. M. Kariuki, A. J. Hallett, S. J. A. Pope, *Dalton Trans.* **2013**, *42*, 10347.

[56] X. Li, X. Tong, Y. Yin, H. Yan, C. Lu, W. Huang, Q. Zhao, *Chem Sci* **2017**, *8*, 5930.

[57] H. A. Al-Attar, G. C. Griffiths, T. N. Moore, M. Tavasli, M. A. Fox, M. R. Bryce, A. P. Monkman, *Adv. Funct. Mater* **2011**, *21*, 2376.

[58] A. P. Wilde, R. J. Watts, *J. Phys. Chem.* **1991**, *95*, 622.

[59] T. S. M. Tang, K. K. Leung, M. W. Louie, H. W. Liu, S. H. Cheng, K. K. W. Lo, *Dalton Trans.* **2015**, *44*, 4945.

[60] G. Moad, E. Rizzardo, S. H. Thang, G. Moad, E. Rizzardo, S. H. Thang, *Aust. J. Chem.* **2005**, *58*, 379.

[61] Y. Luo, Y. Hong, L. Shen, F. Wu, X. Lin, *AAPS PharmSciTech* **2021**, *22*, 1.

[62] J. N. Marhefka, P. J. Marascalco, T. M. Chapman, A. J. Russell, M. V. Kameneva, *Biomacromolecules* **2006**, *7*, 1597.

[63] C. Su, Y. Liu, R. Li, W. Wu, J. P. Fawcett, J. Gu, *Adv. Drug Deliv. Rev.* **2019**, *143*, 97.

[64] P. Sheikholeslami, B. Muirhead, D. S. H. Baek, H. Wang, X. Zhao, D. Sivakumaran, S. Boyd, H. Sheardown, T. Hoare, *Exp. Eye Res.* **2015**, *137*, 18.

[65] V. Baigildin, G. Pankova, T. Evseeva, N. Lavrov, I. Shirokova, G. Vaganov, N. Shevchenko, *J. Dispers. Sci. Technol.* **2017**, *38*, 1570.

[66] J. Wichterlová, K. Wichterle, J. Michálek, *Polymer (Guildf)* **2005**, *46*, 9974.

[67] J. Xu, A. B. Timmons, R. Pelton, *Colloid Polym. Sci.* **2003**, *282*, 256.

[68] G. Kocak, C. Tuncer, V. Bütün, *Polym. Chem.* **2016**, *8*, 144.

[69] J. Y. Lai, Y. T. Li, *Mater. Sci. Eng. C* **2010**, *30*, 677.

[70] M. M. Islam, D. B. Abusamra, A. Chivu, P. Argüeso, C. H. Dohlman, H. K. Patra, J. Chodosh, M. González-Andrades, *Pharmaceutics* **2021**, *13*, 832.

[71] V. Abetz, *Polymers* **2020**, *12*, 794.

[72] L. Kumar, A. Horechyy, E. Bittrich, B. Nandan, P. Uhlmann, A. Fery, *Polymers* **2019**, *11*, 1882.

[73] M. Lim, H. Kwon, D. Kim, J. Seo, H. Han, S. B. Khan, *Prog. Org. Coat.* **2015**, *85*, 68

[74] G. Song, Y. Lin, Z. Zhu, H. Zheng, J. Qiao, C. He, H. Wang, *Macromol. Rapid Commun.* **2015**, *36*, 278.

[75] M. Koivusalo, C. Welch, H. Hayashi, C. C. Scott, M. Kim, T. Alexander, N. Touret, K. M. Hahn, S. Grinstein, *Journal of Cell Biology* **2010**, *188*, 547.

[76] X. Zeng, Y. Zhang, A. M. Nyström, *Biomacromolecules* **2012**, *13*, 3814.

[77] D. Manzanares, V. Ceña, *Pharmaceutics* **2020**, *12*, 371

[78] H. Hillaireau, in *Polymer Nanoparticles for Nanomedicines* (Eds: C. Vauthier, G. Ponchel), Springer International Publishing, Switzerland, 2016 Ch. 10.

[79] J. Bond, J. Varley, *Cytometry A* **2005**, *64A*, 43.

[80] Y. B. Hu, E. B. Dammer, R. J. Ren, G. Wang, *Transl. Neurodegener.* **2015**, *4*, 1.

[81] L. Ma, Q. Ouyang, G. C. Werthmann, H. M. Thompson, E. M. Morrow, *Front. Cell Dev. Biol.* **2017**, *5*, 71.

[82] Z. P. G. Xu, *Pharm. Res.* **2022**, *39*, 1035.

[83] Z. Y. Li, Y. L. Shi, G. X. Liang, J. Yang, S. K. Zhuang, J. bin Lin, A. Ghodbane, M. S. Tam, Z. J. Liang, Z. G. Zha, H. T. Zhang, *ACS Omega* **2020**, *5*, 15911.

[84] I. S. Kritchenkov, V. G. Mikhnevich, V. S. Stashchak, A. I. Solomatina, D. O. Kozina, V. V. Sokolov, S. P. Tunik, *Molecules* **2022**, *27*, 3156.

[85] E. V. Chernikova, P. S. Terpugova, A. N. Filippov, E. S. Garina, V. B. Golubev, A. I. Gostev, E. V. Sivtsov, *Russ. J. Appl. Chem.* **2009**, *82*, 1882.

[86] G. M. Pavlov, O. V. Okatova, A. A. Gosteva, A. S. Gubarev, A. I. Gostev, E. V. Sivtsov, *Colloid Polym. Sci.* **2019**, *297*, 1213.

[87] K. Suzuki, A. Kobayashi, S. Kaneko, K. Takehira, T. Yoshihara, H. Ishida, Y. Shiina, S. Oishi, S. Tobita, *Phys. Chem. Chem. Phys.* **2009**, *11*, 9850.

[88] A. Lobnik, I. Oehme, I. Murkovic, O. S. Wolfbeis, *Anal Chim Acta* **1998**, *367*, 159.

[89] X. Zhang, G.-J. Song, X.-J. Cao, J.-T. Liu, M.-Y. Chen, X.-Q. Cao, B.-X. Zhao, *RSC Adv* **2015**, *5*, 89827.

[90] M. J. Frisch, G. W. Trucks, H. B. Schlegel, G. E. Scuseria, M. A. Robb, J. R. Cheeseman, G. Scalmani, V. Barone, G. A. Petersson, H. Nakatsuji, X. Li, M. Caricato, A. v. Marenich, J. Bloino, B. G. Janesko, R. Gomperts, B. Mennucci, H. P. Hratchian, J. v. Ortiz, A. F. Izmaylov, J. L. Sonnenberg, Williams, F. Ding, F. Lipparini, F. Egidi, J. Goings, B. Peng, A. Petrone, T. Henderson, D. Ranasinghe, V. G. Zakrzewski, J. Gao, N. Rega, G. Zheng, W. Liang, M. Hada, M. Ehara, K. Toyota, R. Fukuda, J. Hasegawa, M. Ishida, T. Nakajima, Y. Honda, O. Kitao, H. Nakai, T. Vreven, K. Throssell, J. A. Montgomery Jr., J. E. Peralta, F. Ogliaro, M. J. Bearpark, J. J. Heyd, E. N. Brothers, K. N. Kudin, V. N. Staroverov,

T. A. Keith, R. Kobayashi, J. Normand, K. Raghavachari, A. P. Rendell, J. C. Burant, S. S. Iyengar, J. Tomasi, M. Cossi, J. M. Millam, M. Klene, C. Adamo, R. Cammi, J. W. Ochterski, R. L. Martin, K. Morokuma, O. Farkas, J. B. Foresman, D. J. Fox, *Gaussian 16, Revision C.01*, *Gaussian, Inc.* Wallingford CT.

[91] R. Peverati, D. G. Truhlar, *Phys. Chem. Chem. Phys.* **2012**, *14*, 16187.

[92] M. Dolg, U. Wedig, H. Stoll, H. Preuss, *J. Chem. Phys.* **1998**, *86*, 866.

[93] I. S. Kritchenkov, P. S. Chelushkin, V. V. Sokolov, V. V. Pavlovskiy, V. V. Porsev, R. A. Evarestov, S. P. Tunik, *Organometallics* **2019**, *38*, 3740.

[94] J. Tomasi, B. Mennucci, R. Cammi, *Chem. Rev.* **2005**, *105*, 2999.

[95] C. Adamo, D. Jacquemin, *Chem. Soc. Rev.* **2013**, *42*, 845.

[96] R. L. Martin, *J. Chem. Phys.* **2003**, *118*, 4775.

[97] T. Lu, F. Chen, *J. Comput. Chem.* **2012**, *33*, 580.

[98] M. Gao, Y. Qin, A. Li, H. Liu, L. Chen, B. Liu, Y. Zhang, Y. Gao, G. Gong, *STAR Protocols* **2021**, *2*, 100543.

[99] B. K. Grillo-Hill, B. A. Webb, D. L. Barber, *Methods Cell Biol.* **2014**, *123*, 429.

[100] Y. Chen, C. Zhu, J. Cen, Y. Bai, W. He, Z. Guo, *Chem. Sci.* **2015**, *6*, 3187.